

DENSE MOLECULAR GAS AND DUSTY TORUS IN NGC 4303

Ángel A. Soní¹, Irene Cruz-González¹, Martín Herrera-Endoqui^{1,2},
Erika Benítez¹, Yair Krongold¹ & Arturo I. Gómez-Ruiz³

Received ; accepted

RESUMEN

El análisis del espectro a 3 mm de la región central de NGC 4303 en un radio de ~ 800 pc, mostró líneas de gas molecular de trazadores de gas denso HCN, HNC, HCO⁺ y C₂H, y de gas difuso ¹³CO y C¹⁸O. Se obtuvieron parámetros del gas molecular: masa del hidrógeno molecular total de la región central, $M_{H_2}=(1.75 \pm 0.32) \times 10^8 M_{\odot}$; velocidad radial de gas denso $V_{dense} = 178 \pm 60 \text{ km s}^{-1}$, y gas difuso $V_{CO} = 151 \pm 29 \text{ km s}^{-1}$ luminosidad de HCN $L_{HCN}=(7.38 \pm 1.40) \times 10^6 K \text{ km s}^{-1} \text{ pc}^2$, masa de gas denso $M_{dense}=(4.7 \pm 0.3) \times 10^7 M_{\odot}$, lo que muestra que el gas denso tiene una contribución significativa a la masa total del gas molecular. Las abundancias de trazadores de gas denso fueron derivados para explorar los procesos físicos que prevalecen en la región nuclear de NGC 4303. Para explorar la naturaleza activa y el toro de polvo central de la galaxia se utilizó CIGALE, para ajustar la distribución espectral de energía integrada de sub-mm al UV. Se estimaron propiedades del toro, como luminosidad $L_{TORUS} = (7.1 \pm 2.8) \times 10^{43} \text{ erg s}^{-1}$ y ángulo de visión $67 \pm 16^\circ$, la cual es consistente con un AGN tipo 2; luminosidad total infrarroja $L_{IR}=(3.5 \pm 0.3) \times 10^{44} \text{ erg s}^{-1}$; tasa de formación estelar $SFR=6.0 \pm 0.3 M_{\odot} \text{ yr}^{-1}$, y se encontró que la contribución del AGN es marginal $\sim 20\%$.

ABSTRACT

Spectrum analysis at 3 mm of the central region ($r \sim 800$ pc) of NGC 4303 showed molecular gas lines of both dense gas tracers (HCN, HNC, HCO⁺, and C₂H) and diffuse gases (¹³CO and C¹⁸O). Molecular gas derived parameters: H_2 mass $M_{H_2}=(1.75 \pm 0.32) \times 10^8 M_{\odot}$; radial velocity $V_{dense} = 178 \pm 60 \text{ km s}^{-1}$, and $V_{CO} = 151 \pm 29 \text{ km s}^{-1}$; HCN luminosity $L_{HCN}=(7.38 \pm 1.40) \times 10^6 K \text{ km s}^{-1} \text{ pc}^2$; dense gas mass $M_{dense}=(4.7 \pm 0.3) \times 10^7 M_{\odot}$, and dense gas tracers abundances indicating that dense gas contributes significantly to the total molecular gas mass. To explore the AGN nature and central dusty torus of the galaxy, CIGALE was used to fit the integrated spectral energy distribution from submillimeter to UV frequencies. Large torus properties are estimated: luminosity $L_{TORUS} = (7.1 \pm 2.8) \times 10^{43} \text{ erg s}^{-1}$ and line of sight inclination of $67 \pm 16^\circ$, which is consistent with a Type 2 AGN; total infrared luminosity $L_{IR}=(3.51 \pm 0.30) \times 10^{44} \text{ erg s}^{-1}$; star formation rate $SFR=6.0 \pm 0.3 M_{\odot} \text{ yr}^{-1}$; and found that the AGN contribution is marginal at $\sim 20\%$.

Key Words: Galaxies: active — Galaxies: ISM — Galaxies: individual (NGC 4303)
— Galaxies: molecular gas

1. INTRODUCTION

Molecular gas characterization of the few central kiloparsecs region of galaxies is important to understand how the gas is accreted into the supermassive black hole (SMBH), and the role of the last one in the host galaxy evolution (e.g. Costagliola et al. 2011; Jiménez-Donaire et al. 2019). The activity in

¹Instituto de Astronomía, Circuito Exterior, C. U., Universidad Nacional Autónoma de México, 04510 CdMx, México.

²Estancia Posdoctoral por México, CONAHCYT, Coordinación de Apoyos a Becarios e Investigadores.

³CONAHCYT-Instituto Nacional de Astrofísica Óptica y Electrónica, Luis E. Erro 1, 72840 Tonantzintla, Puebla, México.

the nuclei of galaxies (AGN) can be dominated by SMBH accretion or starburst (SB) processes, which have different physical and chemical properties that affect their interstellar medium (ISM).

In some AGN the obscuration of the nuclear region by dust and gas is parameterized by the neutral hydrogen column density N_H . Infrared and sub-millimeter observations are less susceptible to dust, especially in the 3 mm window where the brightest emission lines such as HCN or HCO⁺ trace dense molecular gas, whereas the ¹²CO line traces diffuse gas. These lines have proven useful for understanding the central ISM in nearby galaxies (for example, Costagliola et al. 2011; Aladro et al. 2015). On the other hand, in the infrared the dust emission can be observed and studied using broad-band photometry.

Simultaneous observations of ¹²CO isotopic varieties ¹³CO and C¹⁸O of galaxies are valuable for understanding the relationship between the bulk of molecular gas and its environment influenced by the SMBH accretion (e.g., García-Burillo 2016). In addition, these lines are crucial for deriving the gas mass that will be converted into stars.

On the other hand, observations of molecular dense gas tracers such as HCN, HNC, HCO⁺, CS, and N₂H are valuable because their critical densities are of the same order as the molecular cloud cores, which are the star formation sites. Such studies base their analysis on the emission line ratios, for example, HCN/HCO⁺ has been used as a discriminator between AGNs, segregating them into non-Seyfert galaxies (nuclear SB) or pure Seyfert (Sy) galaxies (Kohno 2003). Additionally, HCN/HCO⁺ has been used as an indicator of the presence of AGNs, although this has been challenged several times without conclusive evidence (e.g., Costagliola et al. 2011; Privon et al. 2020). HCN/HNC has been used to characterize photon-dominated regions (PDRs) and X-ray dominated regions (XDRs) (e.g., Meijerink et al. 2007). In addition, both ratios show variations between different galaxy locations such as the center, disk, spiral arms and interarm regions in different studies (e.g., Bigiel et al. 2016; Jiménez-Donaire et al. 2019; Sorai et al. 2019; Morokuma-Matsui et al. 2020). Finally, the dense to diffuse gas ratio HCN/¹²CO associated to star-forming regions is used as a proxy for the dense gas fraction, f_{dense} , as in Neumann et al. (2023).

In the study of dense gas tracers the HCN luminosity (L_{HCN}) can be converted to dense gas mass (M_{dense}), which has been linked by a tight correlation with the far-infrared luminosity, which is closely correlated to the star formation rate (SFR):

$L_{HCN} \propto M_{dense} \propto L_{FIR} \propto SFR$ (see for example, Gao & Solomon 2004a; Jiménez-Donaire et al. 2019; Neumann et al. 2023). This relationship has been observed in individual molecular clouds in the Milky Way and nearby galaxies (Wu et al. 2005; Graciá-Carpio et al. 2006; Bigiel et al. 2008; Wu et al. 2010; Usero et al. 2015; Bigiel et al. 2016; Jiménez-Donaire et al. 2019), and also in few distant galaxies ($z \geq 1$). Before Rybak et al. (2022) only two SF galaxies and three quasar hosts exhibited HCN emissions. These authors showed the difficulties of detecting HCN at $z=2.5-3.3$, but concluded that the HCN/FIR ratios found are consistent with normal starburst galaxies, not ultraluminous ones (c.f., their Figure 5).

Additional information about the properties of the gas in the central kiloparsecs of galaxies can be obtained studying other emission mechanisms that occur inside those spatial scales, such as AGN. According to the Unified AGN model (see Antonucci 1993; Urry & Padovani 1995), the key to distinguishing between Seyfert 1 and 2 galaxies is the existence of a dust structure surrounding the central engine that obscures the inner parts of the AGN on the line of sight (LOS). Based on its geometric shape this structure is called a dusty torus; however, different distributions have been proposed for dust such as that proposed by Fritz et al. (e.g., 2006); Nenkova et al. (e.g., 2008); Hönic & Kishimoto (e.g., 2017). The contribution of the dusty torus luminosity to the integrated spectral energy distribution (SED) could be estimated by an SED fitting analysis (e.g., Ciesla et al. 2015; Miyaji et al. 2019) which yields the dusty torus properties together with the galaxy continuum and line-emitting components, as well as the contribution of the AGN. As part of a study of nearby galaxies with obscured AGN, we analyzed the molecular gas spectra in the 3 mm band of the central, 1.6 kpc in diameter, region of the galaxy NGC 4303 (M 61). NGC 4303 is a barred spiral in the Virgo supercluster at $z=0.00522$ ($D_L = 16.99$ Mpc; $1'' = 81$ pc (Wright 2006)), with an inclination of 25° (Frei et al. 1996), classified as SAB(rs)bc (de Vaucouleurs et al. 1991). Its nuclear activity has been debated, as Huchra et al. (1982) classified it as a LINER, whereas Filippenko & Sargent (1985) as a Seyfert 2, which was confirmed by Veron-Cetty & Veron (1986) based on an equivalent width (EW) of [NII] of 400 km s^{-1} . Jiménez-Bailón et al. (2003) used Chandra images with a central radius of 3 pc and showed that in this X-ray region, both a core source (either an AGN or ultraluminous x-ray source) with hydrogen column density $N_H \sim 1 \times 10^{20} \text{ cm}^{-2}$, and an annular starburst region of radius $3''$ which is more obscured

with $N_H \sim 5 \times 10^{21} \text{ cm}^{-2}$, coexist. The AGN characterization of NGC 4303 was confirmed using an infrared color-color diagram (Colina et al. 2015) and BPT diagrams (Malkan et al. 2017). Furthermore, Esparza-Arredondo et al. (2020) suggested that the nucleus is a candidate for the AGN fading phase.

The AGN contribution in NGC 4303 will be studied by analyzing the continuum emission from UV to far-infrared wavelengths. The dusty torus properties provide important parameters that complement the molecular gas characterization of the central 1.6 kpc region studied in this paper. Our aim is to obtain parameters of the interstellar medium in NGC 4303 such as the molecular gas mass, HCN gas luminosity, far-infrared luminosity and star formation rate.

The remainder of this paper is organized as follows: Section 2 describes the observational details of the 3 mm band spectroscopy. Section 3 presents the data reduction. An analysis of the molecular line emission spectra of NGC 4303 is presented in §4. The spectral energy distribution (SED) characterization to study the dusty torus and AGN contribution is presented in §5. The discussion of results is presented in §6. A summary of the main conclusions and final remarks is presented in §7. Throughout our work we adopt a cosmology where $H_0 = 69.6 \text{ km s}^{-1} \text{ Mpc}^{-1}$, $\Omega_m = 0.286$ and $\Omega_\lambda = 0.714$ (Bennett et al. 2014).

2. OBSERVATIONS

Observations of NGC 4303 were obtained on June 28 and December 22, 2015, with the Redshift Search Receiver (RSR) on the Large Millimeter Telescope Alfonso Serrano (LMT), hereon RSR/LMT, in its early science phase which operated with a 32-m active surface. Observing conditions at the Volcán Sierra Negra site was good most of the time. During the observations the opacity at the Volcán Sierra Negra site at a frequency of 225 GHz was in the range of $\tau = 0.18 - 0.19$. The system temperature, T_{sys} , was in the range of 85 and 110 K. Observations were centered on the coordinates of the galaxy nucleus ($\alpha_{2000}: 12^h:21^m:54^s.9$, $\delta_{2000}: +04^\circ:28':25''$), with the OFF beam 39 arcsec apart. The pointing accuracy was better than $2''$. The total ON source integration time of NGC 4303 was 1 hr.

The RSR is an autocorrelator spectrometer with a monolithic microwave integrated circuit system that receives signals over four pixels, simultaneously covering the frequency range 73 to 111 GHz at $\Delta\nu = 31 \text{ MHz}$ spectral resolution, which corresponds to $\sim 100 \text{ km s}^{-1}$ at 90 GHz (see Erickson et al. 2007). Hence, across the whole 3 mm band, the velocity resolution changes from 125 km s^{-1} to 85 km s^{-1} . The

RSR/LMT-32m has an angular resolution or beam full width at half-maximum (FWHM) that is also frequency dependent, ranging from 28 to 19 arcseconds, between frequencies 73 and 111 GHz.

3. REDUCED SPECTRA

Autocorrelations, spectral co-adding, calibration, and baseline removal were performed using the *Data REduction and Analysis Methods in Python* (DREAMPY) software developed by Gopal Narayanan for the RSR. After removing integrations with unstable bandpass, the remaining spectra were averaged, weighted by the *RMS* noise in each individual spectrum. A simple linear baseline was removed in each spectral chassis, which covered a section of 6.5 GHz of the total RSR bandwidth after masking strong emission lines. To convert the antenna temperature (T_A) units to flux units (Jy), we used a conversion factor G , the gain of the LMT-32m, given by

$$G(\nu) = 7 \left(\frac{\nu [\text{GHz}]}{100 [\text{GHz}]} \right) [\text{Jy K}^{-1}]. \quad (1)$$

The spectral reduction last step was to obtain the main beam temperature (T_{mb}). To convert antenna temperature to T_{mb} , we divided the spectrum by the main beam efficiency (η_{mb})

$$\eta_{mb} = (1.2 \exp(\nu/170)^2)^{-1} \quad (2)$$

where ν denotes the sky frequency of the observed line. Such expression, Eq. (2), was obtained from calibration observations performed in June and December 2015. Details of the RSR/LMT data reduction can be found in several studies, for example Snell et al. (2011); Lee et al. (2014); Yun et al. (2015); Cybulski et al. (2016).

The RSR covers a frequency range of 84 - 111 GHz in the rest frame of NGC 4303. The entire RSR spectrum is shown in Fig. 1, together with the identified lines. The *RMS* of the spectrum varies slightly across the frequency band from 0.618 mK at the low-frequency end ($\nu > 92 \text{ GHz}$) to 0.854 mK at the high-frequency end. Several molecular spectral lines are clearly detected in this spectrum. Using a 3σ detection threshold on the line integrated intensity and rest frequencies from the *Splatalogue*⁴, we detected seven spectral lines: C₂H at 87.31 GHz N=1-0, which is a blend of 6 lines: J=3/2-1/2 (F=1-1, 2-1, 1-0) and J=1/2-1/2 (F=1-1, 0-1, 1-0); HCN(1-0), HCO⁺(1-0), HNC(1-0), CS(2-1), C¹⁸O(1-0), and ¹³CO(1-0) at 88.63, 89.18, 90.66,

⁴<https://splatalogue.online/#/home>

109.78 and 110.20GHz, respectively and the possible detection of three lines: N_2H^+ at 93.17 GHz, NH_2CN at 99.75 GHz and ^{13}CN at 108.65 GHz.

We note that the OFF beam position of the RSR/LMT observations falls within the main body of the galaxy; however, after careful inspection of the reduced data, we found that the $^{13}\text{CO}(1-0)$ spectra do not exhibit an absorption feature, which would appear if the 39 arcsec OFF beam was affected by the OFF galaxy emission. Contamination from the galaxy in the OFF position would be produced by faint CO emission in the spiral arms or inter-arm regions, c.f., PHANGS-ALMA CO(2-1) image of NGC 4303 in Leroy et al. (2021) and would affect all lines, dense and diffuse. This is not found in any of the lines detected, so the contamination, if present, is small.

4. ANALYSIS

4.1. Molecular gas

Seven molecular lines were measured to have integrated line intensity with $S/N > 3$, but CS(2-1) which shows a drop at the low-frequency end, is considered a marginal detection, and so is not considered in the line analysis. For each line, a single Gaussian fit was performed to obtain the integrated intensity, calculated in a range of -250 to $+250$ km s^{-1} , centered on their resting frequencies. The error was computed using the covariance matrix of the fit. The FWHM and peak intensities were obtained using fitting parameters. Individual plots of the detected lines are shown in Fig. 2 and the derived parameters are listed in Table 1.

The most intense line is $^{13}\text{CO}(1-0)$ followed by HCN, HCO^+ and HNC. In a previous study on molecular gas in NGC 4303, Yajima et al. (2019) detected similar integrated intensities than those reported here for $^{12}\text{CO}(1-0)$ and $^{13}\text{CO}(1-0)$ using the Nobeyama 45 m radio telescope, but they were not able to detect $\text{C}^{18}\text{O}(1-0)$. Also, Li et al. (2021) detected the same dense gas tracers lines (HCN, HCO^+ , HNC) with the IRAM 30 m and reported similar integrated measurements to those of this work.

In the following steps, we calculate the mass of the dense molecular gas in the central 1.6 kpc. First, with a combination of optically thin and thick lines, optical depth can be derived. Then, we calculate the column density to finally use it in the calculation of the molecular gas mass. Following Jiménez-Donaire et al. (2017), assuming local thermodynamic equilibrium (LTE), solar abundances and a given excitation temperature in a cloud, the optical depth (τ_{13}) for

^{13}CO can be calculated from the integrated intensities of ^{12}CO and ^{13}CO , I_{12} and I_{13} , respectively. Assuming the beam-filling factor of each line to be the same in the equation of radiative transfer, the optical depth is:

$$\tau_{13} = -\ln \left[1 - \frac{I_{13}}{I_{12}} \right] \quad (3)$$

Because ^{12}CO for NGC 4303 cannot be detected in the frequency range of our observations, we used the value $I_{12} = 55.2 \pm 5.5$ K km s^{-1} obtained with the EMIR spectrograph at the IRAM 30m telescope (FWHM beam size $22''$) reported by Israel (2020) and I_{13} derived from our spectra⁵. By using the values in Eq. (3) yields $\tau_{13} = 0.09 \pm 0.01$, that is, an optically thin line. For ^{12}CO , its optical depth is calculated by multiplying τ_{13} by the relative solar abundance⁶ [$^{12}\text{CO}/^{13}\text{CO}$] = 89 (Wilson & Rood 1994), which yields $\tau_{12} = 7.12 \pm 0.89$; that is, the ^{12}CO line is optically thick.

Now, we used the integrated intensity I_{13} and τ_{13} to obtain the column density N_{13} . Eq. (4) is the result of using the radiative transfer equation to calculate the number of molecules of ^{13}CO over a path length (see eq.1.7 in Jiménez-Donaire 2017):

$$\left[\frac{N_{13}}{\text{cm}^{-2}} \right] = 3 \times 10^{14} \left[\frac{I_{13}}{\text{K km s}^{-1}} \right] \left[\frac{1}{1 - e^{-\tau_{13}}} \right] \frac{\tau_{13}}{1 - e^{-5.29/T_{ex}}} \quad (4)$$

Three excitation temperature (T_{ex}) values commonly found in dense molecular clouds, 10, 20 and 30 K, are assumed in Eq. (4) for the subsequent calculations.

To obtain the mass of H_2 , it was necessary to convert N_{13} to $N(\text{H}_2)$ using the following equation:

$$\left[\frac{N(\text{H}_2)}{\text{cm}^{-2}} \right] = \left[\frac{\text{H}_2}{^{13}\text{CO}} \right] \left[\frac{N_{13}}{\text{cm}^{-2}} \right]. \quad (5)$$

where the relative abundance was $[\text{H}_2/^{13}\text{CO}] = 588,235$ (Dickman 1978). Finally, the H_2 mass was obtained from Eq. (6) assuming a spherical cloud with a diameter calculated for the telescope main beam, which for the ^{13}CO line is $20''$, and that at the NGC 4303 distance corresponds to a diameter $d = 1.647$ kpc and m_{H_2} is the molecular

⁵ The difference in beam size of $3''$ between the two telescopes is small, and might not strongly affect the LMT value of I_{13} used, also it is unlikely that $\tau_{13} > 1$.

⁶ This is the value that most studies assume, but it can vary by a factor of 4.5 between galaxy centers, the local ISM or the solar system.

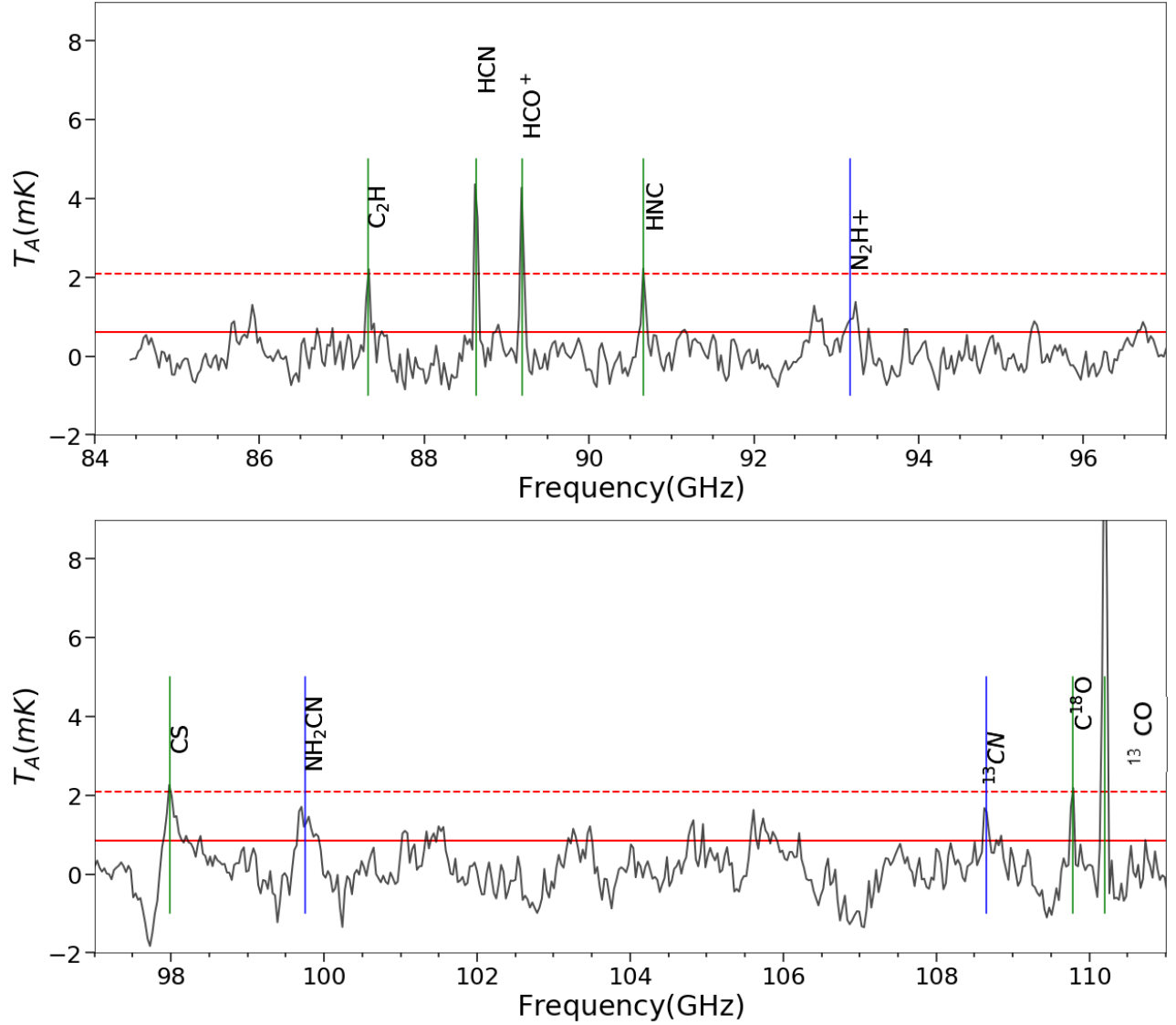


Fig. 1. NGC 4303 rest-frame spectra from 84 to 111 GHz obtained with the Redshift Search Receiver (RSR/LMT). The vertical color lines indicate the likely frequencies of some molecular transitions. The red solid line indicates the root mean square (RMS) value in each panel. The red dashed line represents the value of 3σ . Note that the detected transitions, vertical green lines, are detections of C_2H , HCN, HCO^+ , HNC, CS(2-1), $C^{18}O$, and ^{13}CO , whereas the possible detections in the vertical blue lines are N_2H^+ , NH_2CN and ^{13}CN (see Table 1).

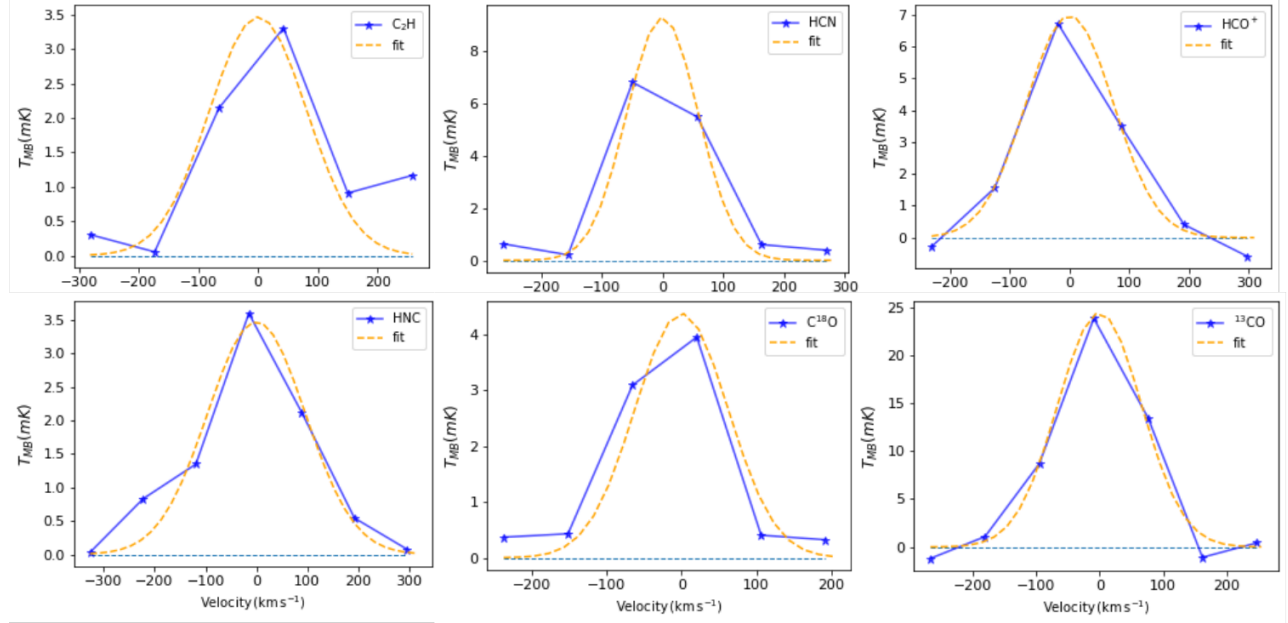


Fig. 2. Observed (blue) molecular lines with $S/N > 3$ of NGC 4303 and their Gaussian fits (orange dashed lines). We detected dense gas tracers as well as ^{12}CO isotopic varieties. From left to right the molecular lines are as follows: (top row) C^2H , HCN , HCO^+ ; (bottom row) HNC , C^{18}O and ^{13}CO .

mass of H_2 .

$$M(\text{H}_2) = \frac{\pi d^2}{4} N(\text{H}_2) m_{\text{H}_2} \quad (6)$$

The derived parameters for NGC 4303 are presented in Table 2, which includes the column densities N_{13} , N_{12} , $N(\text{H}_2)$ and mass $M(\text{H}_2)$ for the three values of T_{ex} .

To obtain the total molecular gas mass (M_{mol}), the contribution of molecular helium to molecular hydrogen must be included in the relationship $M_{\text{mol}} \sim 1.36 M(\text{H}_2)$ from Teng et al. (2022). Therefore, for $T_{\text{ex}} = 30$ K we obtain $M_{\text{mol}} = (2.38 \pm 0.43) \times 10^8 M_{\odot}$. To derive the amount of gas in the observed region, we calculated the surface density of the molecular gas (Σ_{mol}), which is the mass of H_2 per square parsecs area. Taking M_{mol} and the equivalent area of a circle of 1647 pc in diameter, the total surface density of molecular gas is $\Sigma_{\text{mol}} = 112 \pm 20 M_{\odot} \text{pc}^{-2}$.

Using the same procedure as described above, we obtained the total molecular gas mass and surface density of the molecular gas for $T_{\text{ex}} = 10$ K, that is, $M_{\text{mol}} = (9.35 \pm 1.71) \times 10^7 M_{\odot}$ and $\Sigma_{\text{mol}} = 46.5 \pm 8.5 M_{\odot} \text{pc}^{-2}$. Within this range of possible values of T_{ex} , Σ_{mol} varies by a factor of 2.

Usero et al. (2015) calculated the surface density of molecular gas from the intensity of ^{12}CO using the

following equation:

$$\Sigma_{\text{mol}} [M_{\odot} \text{pc}^{-2}] = \alpha_{\text{CO}} I_{12} \cos(i), \quad (7)$$

where i is the inclination of the galaxy, and α_{CO} is the conversion factor of ^{12}CO to molecular gas mass with an adopted value of $4.4 M_{\odot} \text{pc}^{-2} (\text{K km s}^{-1})^{-1}$ (including the 1.36 factor for helium) with a $\pm 30\%$ uncertainty given by Bolatto et al. (2013). Using I_{12} from literature, we obtain $\Sigma_{\text{mol}} = 220 \pm 79 M_{\odot} \text{pc}^{-2}$.

Analogously, we calculated the surface density of the dense molecular gas traced by the HCN line using the equation:

$$\Sigma_{\text{dense}} [M_{\odot} \text{pc}^{-2}] = \alpha_{\text{HCN}} I_{\text{HCN}} \cos(i) \quad (8)$$

where $\alpha_{\text{HCN}} = 10 M_{\odot} \text{pc}^{-2} (\text{K km s}^{-1})^{-1}$, proposed by Gao & Solomon (2004b) is a typical upper limit for spiral galaxies⁷. The result is $\Sigma_{\text{dense}} = 14 \pm 1 M_{\odot} \text{pc}^{-2}$.

We calculate the dense gas mass as traced by HCN, M_{dense} , by multiplying Σ_{dense} by the area of the telescope's main beam, with a diameter of $25''$ for the HCN line. The result is: $M_{\text{dense}} = (4.7 \pm 0.3) \times 10^7 M_{\odot}$.

⁷Leroy et al. (2017) reported an extensive analysis of the use of millimeter-wave emission line ratios to trace molecular gas density. In the dense gas conversion factors, they considered a range of densities for the models as well as the distribution of widths and temperatures

TABLE 1
MOLECULAR LINE TRANSITIONS DETECTED IN NGC 4303

| Molecule | Frequency ^b (GHz) | Integrated Flux (K km s ⁻¹) | Δv^c (km s ⁻¹) | Peak Intensity ^d (mK) |
|------------------------|---------------------------------|--|---------------------------------------|-------------------------------------|
| (1) | (2) | (3) | (4) | (5) |
| C ₂ H(1-0) | 87.31 | 0.77±0.03 | 192±38 | 3.47±0.96 |
| HCN(1-0) | 88.63 | 1.55±0.11 | 138±59 | 9.28±0.97 |
| HCO ⁺ (1-0) | 89.18 | 1.41±0.09 | 171±73 | 6.98±0.97 |
| HNC(1-0) | 90.66 | 0.90±0.04 | 225±48 | 3.47±0.98 |
| CS(2-1) ^a | 97.98 | <2.03±0.68 ^e | – | – |
| C ¹⁸ O(1-0) | 109.78 | 0.77±0.04 | 146±28 | 4.37±1.54 |
| ¹³ CO(1-0) | 110.20 | 4.53± 0.26 | 155±29 | 24.45±1.55 |

Notes:

(a) Possible detection.

(b) Rest frequencies, obtained from the Splatalogue database at <https://splatalogue.online/#/home>.

(c) FWHM in velocity units.

(d) Peak intensity of main beam temperature (T_{MB}).

(e) Upper limit, because line has a blue absorption feature the integrated flux and error result large (see Fig.1).

TABLE 2
COLUMN DENSITIES OF ¹²CO, ¹³CO AND H₂ AND $M(H_2)$

| T_{ex} [K] | N_{13} [$\times 10^{15} \text{cm}^{-2}$] | $N(H_2)$ [$\times 10^{21} \text{cm}^{-2}$] | $M(H_2)^*$ [$\times 10^7 M_\odot$] |
|-----------------|---|---|---|
| 10 | 3.44 ± 0.63 | 2.02 ± 0.37 | 6.88 ± 1.26 |
| 20 | 6.08 ± 1.11 | 3.58 ± 0.65 | 12.17 ± 2.23 |
| 30 | 8.74 ± 1.60 | 5.14 ± 0.94 | 17.50 ± 3.20 |

Note:

* $M(H_2)$ was calculated from Eq. (6).

Finally, with Σ_{dense} and Σ_{mol} for $T_{ex} = 30$ K, we can calculate the dense molecular fraction (f_{dense}) in the observed region as:

$$f_{dense} = \frac{\Sigma_{dense}}{\Sigma_{mol}} = 0.13 \pm 0.06 \quad (9)$$

4.2. Luminosities

Gao & Solomon (2004b) calculated the luminosity of an extended source with a size larger than the main beam of the telescope. Because the galaxy is not mapped on the major axis, it is considered a source with a size equal to or smaller than the tele-

scope's main beam. The calculation is given by:

$$L'_{HCN} [K km s^{-1} pc^2] \approx \Omega_{mb} I_{HCN} D_L^2 (1+z)^{-3} \quad (10)$$

where Ω_{mb} is the solid angle of the main beam, D_L (pc) is the luminosity distance, I_{HCN} is the integrated HCN line intensity and z is the *redshift*. We can rewrite Ω_{mb} in terms of the antenna parameters, that is, the FWHM of the main beam θ_{FWHM} (in radians) and obtain the HCN luminosity as

$$L'_{HCN} [K km s^{-1} pc^2] \approx \frac{\pi}{4 \ln(2)} \theta_{FWHM}^2 I_{HCN} D_L^2 (1+z)^{-3}. \quad (11)$$

We then calculate the luminosity of the dense gas tracers substituting the integrated intensities of this work, e.g., HCN by HCO^+ and the corresponding values of θ_{FWHM} at the observing frequency, $\sim 25''$ for the dense gas tracers and $20''$ for ^{13}CO (see Table 3).

If we use the mass-luminosity conversion factor defined as $\alpha_{^{13}\text{CO}}$ with units $\text{M}_{\odot} \text{pc}^{-2} (\text{K km s}^{-1})^{-1}$, one can rewrite the Solomon relation (Solomon et al. 1997) as $M(H_2) = \alpha_{^{13}\text{CO}} L'_{13}$ or

$$\alpha_{^{13}\text{CO}} = \frac{\Sigma_{H_2}}{I_{13}}. \quad (12)$$

Using the previously calculated data for $M(H_2)$, $\Sigma_{H_2} = 82 \pm 15 \text{ M}_{\odot} \text{pc}^{-2}$ and Eq. (12), we calculated both the factor $\alpha_{^{13}\text{CO}}$ and the ^{13}CO luminosity, resulting $\alpha_{^{13}\text{CO}} = (18.2 \pm 4.4) \text{ M}_{\odot} \text{pc}^{-2} (\text{K km s}^{-1})^{-1}$ and $L'_{13} = (9.6 \pm 3.9) \times 10^6 \text{ K km s}^{-1} \text{pc}^2$. The ^{12}CO luminosity is calculated with the Eq. (7) and the FWHM of $22''$ of the observed line, which results in $L'_{12} = 1.29 \times 10^8 \text{ K km s}^{-1} \text{pc}^2$.

To estimate the abundance of molecular gas in the nuclear obscured region, we used the integrated intensity of the different emission lines of dense gas tracers (C_2H , HCN, HNC and HCO^+), diffuse gas tracers (^{13}CO , C^{18}O) and ^{12}CO integrated intensity $I_{12} = 55.2 \pm 5.5 \text{ K km s}^{-1}$ (Israel 2020) to calculate their line ratios (Table 4).

4.3. Dusty torus, SFR and AGN contribution to the SED

As mentioned in § 1, previous multiwavelength studies confirmed that the nuclear activity of NGC 4303 is influenced by an accreting SMBH (Filippenko & Sargent 1985; Veron-Cetty & Veron 1986; Malkan et al. 2017; Colina et al. 2015), classifying it as Sy 2 (Véron-Cetty & Véron 2006). In this work we are also interested in the physical properties of NGC 4303, mainly the star formation rate (SFR), in order to compare the values derived here with those from the literature. A good tool to achieve this task is integrated spectral energy distribution (SED) fitting analysis, which includes an AGN component. Interestingly, this complementary analysis allows us to obtain not only the galactic properties but also the AGN properties, including dusty torus characteristics. All these properties are useful for follow-up studies.

For this purpose, we used the Code Investigating GALaxy Evolution, called CIGALE, developed by Boquien et al. (2019), which allows fitting of the SED of galaxies using different models for the relevant physical components. For instance, it is possible

to select from different star-forming history models, stellar populations, initial mass functions, attenuation laws, dust emissions and AGN models. The different components are fitted to preserve the energy balance principle, which means that the energy absorbed at UV and optical wavelengths is re-emitted at infrared wavelengths. To select the best fit, CIGALE performs a minimization of the χ^2 statistics and performs Bayesian analysis to determine the probability distribution of the physical parameters obtained from the fits.

We searched for photometric data of NGC 4303 in the literature, using the Vizier photometry tool⁸, which allows visualization of photometric points extracted from catalogues in ViZier around a sky position. We used a default search radius of $5''$ centered at NGC 4303, which is small enough to consider data truly corresponding to the emission of the galaxy, finding multi-wavelength observations at UV, optical, infrared and sub-millimeter wavelengths (see Table 5). According to de Vaucouleurs et al. (1991), the isophotal dimensions (R_{25}) of NGC 4303 are $6'.46 \pm 0'.15$ and $5'.75 \pm 0'.27$, for the major and minor axes, respectively. This means that all the observations retrieved from the literature include the total emission of the galaxy.

The UV data consist of Galaxy Evolution Explorer (GALEX; Martin et al. 2005) observations in the far-ultraviolet (FUV; $\lambda_{\text{eff}} = 0.153 \mu\text{m}$) and near-ultraviolet (NUV; $\lambda_{\text{eff}} = 0.231 \mu\text{m}$) bands with an angular resolution of $5''.3$ and $1''.2$ field of view (FOV), taken from Cortese et al. (2012). The optical data consist of observations from the Sloan Digital Sky Survey Data Release 7 (SDSS-DR7; Abazajian et al. 2009) in the five bands u , g , r , i and z , taken from Kim et al. (2014). These data have an angular resolution of $\leq 1''.5$, and 3° FOV. In the IR regime we compiled data from different sources: the Two Micron All Sky Survey (2MASS; Skrutskie et al. 2006), the *Spitzer* Space Telescope (Werner et al. 2004), the Infrared Astronomical Satellite (IRAS; Neugebauer et al. 1984), the Wide-field Infrared Survey Explorer (WISE; Wright et al. 2010), and the *Herschel* Space Telescope (Pilbratt et al. 2010). In the case of 2MASS data, we use photometry in the J ($1.2 \mu\text{m}$), H ($1.6 \mu\text{m}$) and K ($2.2 \mu\text{m}$) bands from Bai et al. (2015), Dalya et al. (2016) and Stassun (2019), respectively, all of them with an angular resolution of $2''$ and a $8^\circ 5'$ FOV. In the case of *Spitzer* data, we considered observations obtained with the InfraRed Array Camera (IRAC; Fazio et al. 2004)

⁸<http://vizier.cds.unistra.fr/vizier/sed/doc/>

TABLE 3
LUMINOSITIES FOR DIFFUSE AND DENSE GAS EMISSION LINES IN NGC 4303.

| Line | L_{gas} $\times 10^6 [K km s^{-1} pc^2]$ | $\log(L_{gas})$ $[K km s^{-1} pc^2]$ |
|-------------|---|---|
| ^{13}CO | 9.60 ± 3.90 | 6.98 ± 0.09 |
| C_2H | 3.78 ± 0.68 | 6.58 ± 0.07 |
| HNC | 7.38 ± 1.40 | 6.87 ± 0.08 |
| HCO^+ | 6.63 ± 1.24 | 6.82 ± 0.08 |
| HNC | 4.09 ± 0.75 | 6.61 ± 0.08 |
| Total dense | 21.88 ± 4.07 | 7.34 ± 0.08 |

TABLE 4
ABUNDANCES OF DENSE GAS RELATIVE TO
DIFFUSE AND DENSE GAS TRACERS.

| Ratio* | Value |
|---------------------|-------------------|
| $C_2H / C^{18}O$ | 1.01 ± 0.07 |
| $HNC / C^{18}O$ | 2.01 ± 0.18 |
| $HCO^+ / C^{18}O$ | 1.83 ± 0.15 |
| $HNC / C^{18}O$ | 1.17 ± 0.08 |
| $CS / C^{18}O$ | 2.67 ± 0.19 |
| $^{13}CO / C^{18}O$ | 5.88 ± 0.46 |
| $HNC / ^{12}CO$ | 0.028 ± 0.002 |
| $HCO^+ / ^{12}CO$ | 0.025 ± 0.003 |
| $HNC / ^{12}CO$ | 0.016 ± 0.003 |
| $^{13}CO / ^{12}CO$ | 0.082 ± 0.010 |
| $C^{18}O / ^{12}CO$ | 0.013 ± 0.002 |
| HNC / HCN | 0.58 ± 0.04 |
| HCO^+ / HCN | 0.91 ± 0.08 |
| C_2H / HCN | 0.38 ± 0.04 |

Note: * For ^{12}CO we used $I_{12} = 55.2 \pm 5.5 K km s^{-1}$ (Israel 2020).

in the IRAC1 (3.6 μm), and IRAC2 (4.5 μm) bands from Sheth et al. (2010), and IRAC4 (8 μm) band from Ciesla et al. (2014). These data have resolution of 1''.7, 1''.6, 1''.9, respectively, with a 5' FOV for IRAC1 and IRAC2 bands, and 5'.2 \times 5'.2 in the case of IRAC4. In the case of IRAS data, we use the photometry in the 12 μm band from Moustakas & Kennicutt (2006), the 25 and 60 μm bands from Rahman et al. (2006), and the 100 μm band from Yun et al. (2001), with a resolution of 0'.5, 0'.5, 1'.0 and 2'.0, respectively, and a common 63'.6 FOV. We

also consider data in the MIPS 24 and 160 μm bands from Bendo et al. (2012), whose angular resolution is 6'' with a 5'.4 \times 5'.4 FOV. From WISE, we use observations in the W1 (3.4 μm) and W2 (4.6 μm) bands from Stassun (2019), the W3 (12 μm) band from Ciesla et al. (2014), and the W4 (22 μm) band from Boselli et al. (2014). These data have angular resolution of 6''.1, 6''.4, 6''.5, 12''.0, respectively, and a common 47' FOV. In the case of *Herschel* data, we use observations obtained with the Photodetector Array Camera and Spectrometer (PACS; Poglitsch et al. 2010), in the 100 μm (PACSgreen) and 160 μm (PACSred) bands with angular resolution of 8'' and 13'', respectively, and a 3'.5 \times 1'.75 FOV, as well as the Spectral and Photometric Imaging Receiver (SPIRE; Griffin et al. 2010), in the 250 μm (PSW), 350 μm (PMW) and 500 μm (PLW) bands with angular resolution of 18'', 25'' and 36'', with a 8'.0 \times 4'.0 FOV. PACS data were collected from Auld et al. (2013), whereas the SPIRE data were collected from Chen et al. (2018). Finally, we used observations taken with the Submillimeter Common-User Bolometer Array (SCUBA; Holland et al. 1999) instrument on the James Clerk Maxwell Telescope (JCMT). These observations in the 850 μm band were taken from Di Francesco et al. (2008) with angular resolution of 22''.9 and a 2'.3 FOV.

We fitted the SED of NGC 4303 using typical choices of the components to fit for galaxies harbouring an AGN (e.g. Wang et al. 2020; Santos et al. 2021), a delayed star formation history with an optional exponential burst and stellar populations model by Bruzual & Charlot (2003) using the `sfhdelayed` module with a Chabrier (2003) initial mass function (`bc03`). We considered nebular emission to account for any Lyman continuum emission (`nebular`). The attenuation law (`dustatt_modified_starburst`) is that of Calzetti

et al. (2000), whereas the dust emission is modeled using Jones et al. (2017) models (**themis**). For the AGN component we use the CLUMPY⁹ models through the **nenkova2008** module, which considers the emission from a clumpy torus (Nenkova et al. 2008a,b). This latter module has recently been used successfully in other SED fitting studies of AGNs given its flexibility regarding the geometrical parameters of the torus (Miyaji et al. 2019; Yamada et al. 2023). Each of the aforementioned modules, corresponding to the physical components, has its own parameters that can take several values to form the grid of models to be fit to the SED. The physical components, corresponding modules, parameters, and values adopted in this analysis are listed in Table 6.

In Figure 3 we present the best fit for the NGC 4303 SED. The observed fluxes (purple circles), model fluxes (red circles), and total model (black line) are shown. The different physical components used were as follows: the stellar component before (yellow line) and after attenuation (blue dashed line), dust emission (red line), nebular emission (green lines), and AGN component (apricot line). The flux residuals in each band are shown in the bottom panel and are calculated as $(S_{\nu, \text{obs}} - S_{\nu, \text{model}})/S_{\nu, \text{obs}}$. The reduced χ^2 of the fit was 3.1.

Regarding the geometrical parameters of the clumpy dusty torus obtained with the best fit and the Bayesian analysis values (in parenthesis), we obtained a thick torus given its aperture above the equatorial plane **op_angle** = 60° ($56^\circ \pm 9^\circ$), a large optical depth **tau.V**=200 (184 ± 38), a large number of clouds along the equatorial plane **N_0**=15 (14 ± 2), and an inner to outer radius ratio of **Y_ratio**=100 (97 ± 12). The power of the radial distribution of clouds ($\propto r^{-q}$) is **q**=0.0 (0.12 ± 0.29) and the viewing angle is **incl**= 80° ($67^\circ \pm 16^\circ$). By considering the classical unified AGN model (Antonucci 1993; Urry & Padovani 1995). This viewing angle is in agreement with the Sy 2 classification of Véron-Cetty & Véron (2006).

The total AGN and torus luminosities of the best fit and the Bayesian analysis values (in parenthesis) are $L_{\text{AGN}} = 1.5 \times 10^{44} \text{ erg s}^{-1}$ ($(1.5 \pm 0.6) \times 10^{44} \text{ erg s}^{-1}$), $L_{\text{TORUS}} = 6.975 \times 10^{43} \text{ erg s}^{-1}$ ($(7.1 \pm 2.8) \times 10^{43} \text{ erg s}^{-1}$), while the galaxy dust luminosity is $L_{\text{DUST}} = 2.8 \times 10^{44} \text{ erg s}^{-1}$ ($(2.8 \pm 0.1) \times 10^{44} \text{ erg s}^{-1}$), and the total IR luminosity is $3.5 \times 10^{44} \text{ erg s}^{-1}$ ($(3.51 \pm 0.30) \times 10^{44} \text{ erg s}^{-1}$). Another important quantity derived from CIGALE is the star formation rate, which in this case is $SFR = 6.014 M_\odot \text{ yr}^{-1}$ ($5.969 \pm 0.298 M_\odot \text{ yr}^{-1}$). The parameters derived

from CIGALE are presented in Table 7.

5. DISCUSSION

5.1. Dense and Diffuse Gas Masses and Kinematics

The molecular hydrogen mass obtained for the telescope's main beam center in line ^{13}CO can be compared with that found by Schinnerer et al. (2002) in a high spatial resolution study ($\sim 150 \text{ pc}$) of gas traced by ^{12}CO (J=1-0) line made with the *Owens Valley Radio Observatory* (OVRO). As can be seen in Fig. 4, the molecular gas emission is found in two lanes: the western gas lane (LW) and the eastern gas lane (LE), both curving towards the nucleus (N). It was found that the central $8''$ ($\sim 630 \text{ pc}$) concentrates a mass $M(H_2) \sim 7 \times 10^7 M_\odot$. Their estimation used the conversion factor $\alpha_{CO} = 4.36 M_\odot \text{ pc}^{-2} (\text{K km s}^{-1})^{-1}$ from Strong et al. (1988), with a $\pm 30\%$ uncertainty. In addition, the southern component of LW and the north component of LE that extend to an area of $\sim 22'' \times 22''$, concentrate almost twice the value of the nuclear disk or central $8''$ mass, see Table 3 in Schinnerer et al. (2002). Consequently this yields a total central molecular mass $M(H_2) \sim 1.81 \times 10^8 M_\odot$. If we use instead the integrated intensity of the ^{12}CO (J=1-0) line obtained from literature (Israel 2020), the molecular mass associated with this line derived from $\Sigma_{mol} = 220 \pm 79 M_\odot \text{ pc}^{-2}$ (see §4.1), for an area with a diameter of $22''$ ($\sim 1.8 \text{ kpc}$) is $(5.7 \pm 2.0) \times 10^8 M_\odot$. Using the same conversion factor α_{CO} in both calculations, the factor of 3 difference in both masses could be due to the spatial resolution with which the observations were made, a beam of $\sim 150 \text{ pc}$ vs. $\sim 1.8 \text{ kpc}$. In the second case, assuming a constant beam filling factor overestimates the amount of emission within the observed area.

In this study, the calculated molecular H_2 mass was $M(H_2) = (1.75 \pm 0.32) \times 10^8 M_\odot$, which is in good agreement with the value reported by Schinnerer et al. (2002). We note that although the RSR/LMT observed region (the circle of $20'' \sim 1.6 \text{ kpc}$ of diameter) does not completely cover the arms as shown in Fig. 4, most of the molecular gas is concentrated in the central region, which explains the similar values. Schinnerer's work covers a slightly larger area than the one presented here, so to properly compare $M(H_2)$, we consider the value from Schinnerer et al. (2002) presented above as an upper limit.

As we saw in the previous section, the $M(H_2)$ value obtained with ^{12}CO and Eq. (7) is three times the value obtained with ^{13}CO . This difference may be due to the conversion factor α_{CO} , as although in many studies it is assumed to be a constant value

⁹<https://clumpy.org/>

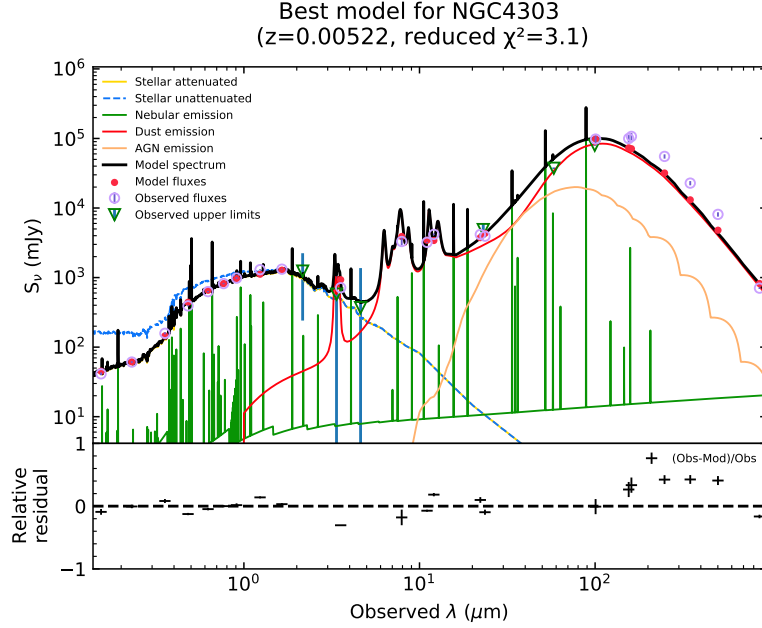


Fig. 3. The best SED model fit for NGC 4303 using CIGALE. Shown are the observed fluxes (purple circles), model fluxes (red dots), total model (black line), unattenuated stellar emission (blue line), attenuated stellar contribution (yellow line), nebular emission (green line), dust emission (red line) and AGN emission (orange line). The bottom panel shows the residuals of the observed to the model fluxes.

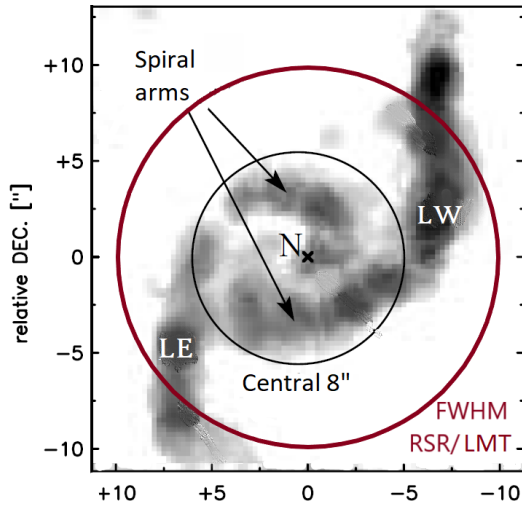


Fig. 4. A high spatial resolution (~ 150 pc) map of the center of NGC 4303 observed with OVRO in the ^{12}CO (1-0) line obtained by Schinnerer et al. (2002) covering $22'' \times 22''$. The center (black circle) has a diameter of $8''$, and the red circle is RSR/LMT region of $20''$ which represents the LMT main beam for ^{13}CO frequency. The bulk of molecular gas in this region obtained by Schinnerer et al. (2002) was compared with that obtained in our study using the ^{13}CO line.

across various scales and environments, recent studies have found variations of 1-2 orders of magnitude that depend on the physical properties of the medium. Teng et al. (2023) observed the central ~ 2 kpc region of two barred spiral galaxies at ~ 100 pc resolution with ^{12}CO and found a correlation between α_{CO} and the optical depth, an anticorrelation with kinetic temperature of the gas and low values of α_{CO} by factors of 4-15 in the central regions of these galaxies. As we can see, this variation has a significant impact on the calculation of molecular masses and the quantities derived from it, so care must be taken in choosing the value of α_{CO} according to the scale and characteristics of the ISM. In this paper, we consider the value of $M(\text{H}_2)$ obtained with ^{13}CO to be the most accurate.

The surface density of dense molecular gas (Σ_{dense}) obtained using Eq. (8) is integrated in a region where the molecular gas is not homogeneously distributed and thus Σ_{dense} may be underestimated (see Fig. 4). An important result is the calculation of the amount of dense gas traced by the HCN in the same region $M_{\text{dense}} = (4.7 \pm 0.3) \times 10^7 M_{\odot}$. This value resulted ~ 4 times smaller than the total mass of molecular hydrogen. This dense star-forming gas provide the conditions for the 200–250 pc diameter circumnuclear ring studied by Riffel et al. (2016),

through observations in the UV-optical-IR, where they reveal intense bursts of star formation. The relationship between dense and molecular mass is $M_{dense}=0.21 M(H_2)$ which is comparable to $f_{dense}=0.13\pm 0.06$, within the uncertainties.

Regarding gas kinematics, we analyzed the velocity of the molecular emission lines and compared them with those in previous studies. The rotational curve of the galaxy traced by molecular gas ^{12}CO $J=(2-1)$ with a resolution of ~ 150 pc from ALMA observations (Figure D3, Lang et al. 2020) shows the fitting of the observational data, resulting in asymptotic rotation velocity $V_0 = 178.2^{+75.1}_{-43.0}$ km s^{-1} . Meanwhile, the curves obtained by simulations of central bar formation made by Iles et al. (2022), show that, for a $r \leq 2$ kpc radius, the rotational velocity V_{rot} from the simulations (IsoB IC, blue curves in Figure A1 in that paper) are in the range of 150 to 175 km s^{-1} .

In this study, the velocities for the diffuse gas, i.e., ^{13}CO and C^{18}O , gave us a mean velocity of $V_{CO} = 151 \pm 29$ km s^{-1} that matches with the rotational velocity in the $r \leq 2$ kpc radii obtained by Iles et al. (2022), i.e., which covers partially the bar radius $r_{bar} = 2.50 \pm 0.63$ kpc (e.g., Zurita et al. 2021), which is important because in this region the bar dominates the gas kinematics. Meanwhile, the mean value of the velocity for dense gas tracers HCN, HNC, and HCO^+ is $V_{dense} = 178 \pm 60$ km s^{-1} , which is consistent with the results obtained by Lang et al. (2020). The dense gas velocity is comparable with the diffuse gas even having different FOVs, this is maybe due to the dominance of the structural component of the bar.

5.2. Emission line ratios

The molecular emission line ratio method helps quantify the molecular gas in specific regions of the galaxy, as in the case of AGN, and can provide information to characterize the star formation or SMBH accretion processes. In this work, we are trying to determine if the presence of the AGN is hinted by the line ratios and to characterize the ISM from this central 1.6 kpc region.

Previous studies have attempted to classify the activity of galaxies using molecular emission line diagrams such as HNC/HCN or highest values of HCN/ HCO^+ (Kohno et al. 2001; Costagliola et al. 2011; Jiang et al. 2011).

Another example is the use of the HNC/HCN ratio as an indicator of shock and non-standard heating, or the CS/HCN ratio, which should be greater than 1 at high column densities for both XDRs and

PDRs, suggesting a correlation with column density (Baan et al. 2008).

Jiménez-Donaire et al. (2019) studied dense gas in nine nearby galaxies at $\sim 1-2$ kpc resolution and showed that the main emission line ratios had a maximum value at the center (with radius ≈ 0.8 kpc) and decreased radially towards the outermost parts of the disk or spiral arms. Using values from Jiménez-Donaire et al. (2019) and our study, we present in Fig. 5 the diagnostic diagram of HNC, HCN, HCO^+ relative to ^{12}CO . We observed an increasing relationship that clearly separated the galaxy regions, with the galactic centers being the most intense. The ratios HCN/ ^{12}CO , $\text{HCO}^+ / ^{12}\text{CO}$ and HNC/ ^{12}CO presented in Table 4 for the center of NGC 4303 are located in the diagnostic diagram as mentioned previously. As shown, our values are located in the region where the galactic central regions are also located. It should be noted that the center of the galaxy closest to our point is the barred spiral galaxy NGC 6946, which is also classified as a Sy 2.

The ratio between ^{12}CO and ^{13}CO is denoted by $R_{12/13}$ and has been studied for a large sample of galaxies because these lines are generally more intense and easier to detect (e.g., Aladro et al. 2015; Israel 2020). The value $R_{12/13}$ for the nucleus of the galaxy NGC 4303 is 12.1 ± 1.4 , consistent with the mean value $R_{12/13} = 13 \pm 6$ of nearby starburst galaxies found by Aalto et al. (1995). This ratio provides information on the variation in optical depth in each galaxy, as well as the relative abundances of ^{12}C and ^{13}C . In the case of ^{12}C , this can be produced by supernovas of massive stars, whereas ^{13}C can be produced in low-mass stars or ion exchange $^{13}\text{C}^+$ in regions with temperatures ~ 10 K (see, for example, Keene et al. 1998; Davis 2014).

The HNC/HCN = 0.58 ± 0.04 ratio shows that HNC abundance is lower than that of HCN. Hirota et al. (1998) observed 19 nearby dark cloud cores with Nobeyama 45 m. According to them, the HNC/HCN value is a consequence of the temperature of the central molecular region $T_{ex} > 24$ K, where neutral-neutral reactions occur. In this manner, the HNC molecule is destroyed to form its isomer, HCN. This supports the use of $T_{ex} = 30$ K to derive surface densities with the corresponding value of $M(H_2)$.

HCN/ HCO^+ is the ratio most sensitive to density changes, because the critical density of HCO^+ is one order of magnitude smaller than that of HCN. Therefore, HCO^+ tends to recombine faster than HCN, when the medium is dense owing to free electrons. However, both molecules have similar abun-

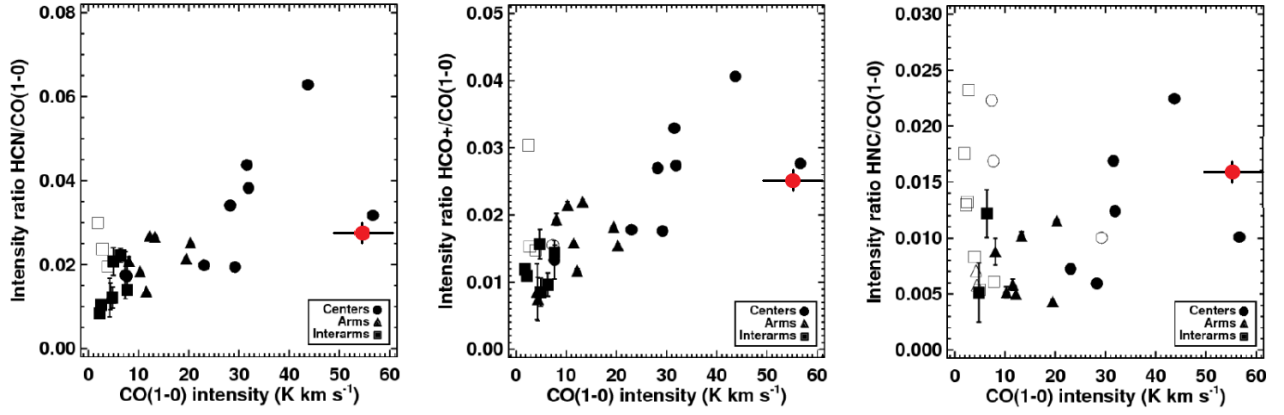


Fig. 5. Diagnostic diagrams left-to-right $\text{HCN}/^{12}\text{CO}$, $\text{HCO}^+ / ^{12}\text{CO}$ and $\text{HNC}/^{12}\text{CO}$ for a sample of nine nearby galaxies from Jiménez-Donaire et al. (2019). Squares are the values in the interarms regions, triangles are the values in the arms and circles are the values of the centers of these galaxies. Open symbols represent upper limits. The red circles represent the values for the central region of NGC 4303 obtained in this study, which is consistent with the location of the centers of other spiral galaxies on the diagram.

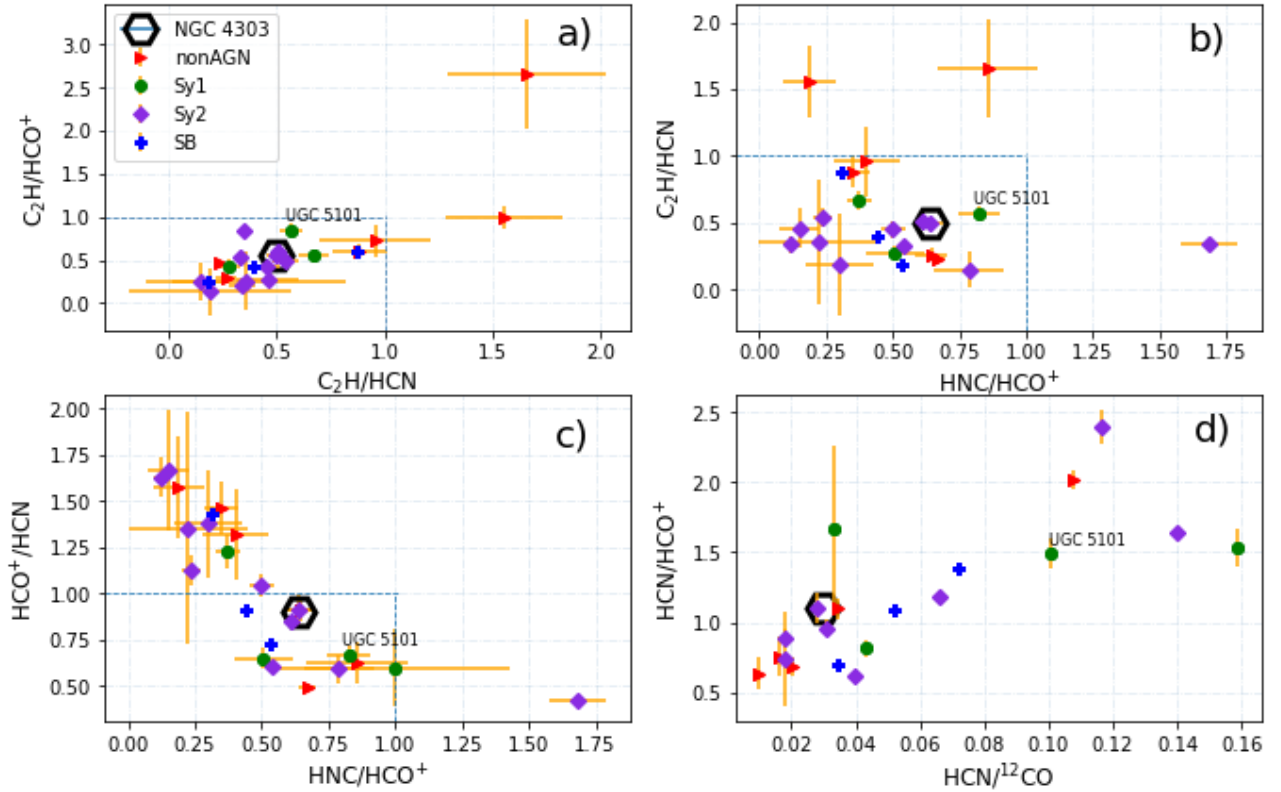


Fig. 6. Line ratio diagrams for a set of 22 galaxies in the literature plus central 1.6 kpc of NGC 4303. Left to right: a) $\text{C}_2\text{H}/\text{HCO}^+$ vs. $\text{C}_2\text{H}/\text{HCN}$, b) HNC/HCO^+ vs. $\text{C}_2\text{H}/\text{HCN}$, c) HNC/HCO^+ vs. HCO^+/HCN , d) $\text{HCN}/^{12}\text{CO}$ vs. HNC/HCO^+ . The line ratio values from the literature are integrated values, the open black hexagons are the values for the central 1.6 kpc of NGC 4303. In addition, the values for UGC 5101 obtained by Cruz-González et al. (2020) in a similar study are labeled in each diagram. The dashed blue line enclosed is the region where the ratio is less than one.

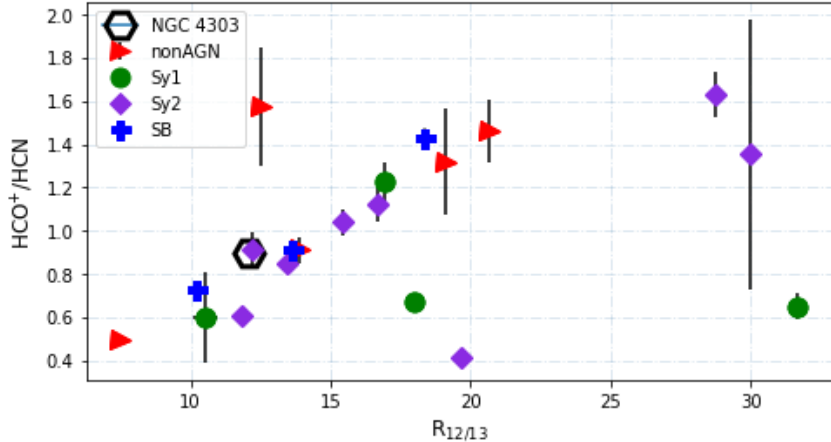


Fig. 7. $R_{12/13}$ vs. HCO^+/HCN for a sample of 12 nearby galaxies. The open black hexagon is the value for the center of NGC 4303. Although a clear linear dependence can be seen between the lines, there is no dependence on galactic activity.

dances, indicating that at high densities there is possibly a mechanism that enhances the abundance of HCO^+ . Studies of molecular abundance by Meijerink & Spaans (2005) suggests that, in PDRs, this molecule abundance enhancement occurs at densities $n > 10^5 \text{ cm}^{-3}$. As mentioned previously, HCN/HCO^+ has also been used to determine the nature of the nuclear-emitting source. In particular, values of HCN/HCO^+ greater than one, were found in XDRs, caused by AGN with low density $n > 10^4 \text{ cm}^{-3}$ and $N(\text{H}_2) < 10^{22} \text{ cm}^{-2}$ (for example, Loenen et al. 2008), which agrees with the values of $\text{HCN}/\text{HCO}^+ = 1.10$ and $N(\text{H}_2)$ found in our study (see Table 2). Recently, Nishimura et al. (2024) found in a 23 local ULIRGs sample than this ratio (J=3-2 lines) have no trend with AGN luminosity or implication in SFR, but the presence of outflows or inflows have the most crucial influence. The HCN/HCO^+ ratio indicates a very similar abundance between the two molecules. Thus, HCO^+ can form in the dense region, that is, when $n_{\text{critic}} > 10^5 \text{ cm}^{-3}$, ionization must occur in the medium through shock waves or PDRs produced by young stars. The stellar populations of the circumnuclear region described by Dametto et al. (2019) are young ($t < 2 \text{ Gyr}$) and add a high density to the medium, reinforcing the idea that the gas in the region has high ionization probabilities for radical formation.

Recently, Neumann et al. (2023) presented the results of the ALMOND (ACA Large-sample Mapping Of Nearby galaxies in Dense gas) survey, where they traced the molecular gas density using resolved measurements of $\text{HCN}(1-0)$ across 25 nearby spiral galaxies, one of which was NGC 4303. The HCN

beam in that work ($20'' \sim 1.6 \text{ kpc}$) is similar to ours, and therefore, the results can be compared. The HCN integrated intensity in the 2 kpc galactocentric radius, had a peak temperature of 9.4 mK, similar to our value (see Table 1). In the upper left panel of Figure 6 of Neumann et al. (2023), the relationship between $\text{HCN}(1-0)/^{12}\text{CO}(2-1)$ and (Σ_{mol}) is presented, our logarithmic values are -1.55 and 2.05, respectively, which lie in their linear relation. This data point is within the range of values for $\log \text{HCN}/^{12}\text{CO}$ reported for NGC 4303 (see their figure I4). Our Σ_{mol} is on the lower end of the range reported in Neumann et al. (2023), but we note their value was calculated as a cloud-scale property at 150 pc resolution using α_{CO} , whose uncertainty can be attributed to variations in the galactocentric radius (e.g., Sandstrom et al. 2013).

Diagnostic diagrams were constructed to determine possible relationships between type of galaxy activity and emission lines. In Table 8 we present a sample of 23 normal main sequence, starburst (SB), AGN Sy 1 and AGN Sy 2 galaxies with integrated intensities of HCN, HNC, C_2H , HCO^+ , ^{12}CO and ^{13}CO reported in the literature. The sample is presented in Figure 6, and includes the values for the central region of NGC 4303 as a black circle. In these diagrams no relationship between the line intensity ratios and galaxy activity is observed, the SB types and AGNs are mixed, and NGC 4303 lies between the groups. Linearity trends can be observed between the ratios: $\text{C}_2\text{H}/\text{HCN}$ vs. $\text{C}_2\text{H}/\text{HCO}^+$, HNC/HCO^+ vs. HCO^+/HCN and $\text{HCN}/^{12}\text{CO}$ vs. HCN/HCO^+ .

In the first relation, (a) in Fig. 6, we can see a

linear relation between these ratios, also the majority of the galaxies lie in the region where the ratios are less than one, with the especial cases of NGC 3556 and IC 180. The diagram (d) $\text{HCN}/^{12}\text{CO}$ vs. HCN/HCO^+ shows an increasing relation too, where, for values of HCN/HCO^+ less than one, most of the galaxies have a low fraction of dense gas ($\lesssim 0.05$) and for values greater than one the amount of dense gas, with respect to diffuse gas grows by a factor of 5-8. This last point may indicate a strong relationship between HCO^+ and CO. Additionally, having a dense gas fraction greater than 5% may be linked to the recombination of HCO^+ and increase the abundance of HCN molecules.

Regarding the presence of C_2H in the central region may be associated with reactions produced by PDRs in massive, hot star formation regions (for example, Martín, S. et al. 2015). This molecule, like other simple hydrocarbons (^{13}CN , CH, $c\text{-C}_3\text{-H}_2$) are the product of keeping a large amount of carbon ionized with warm gas associated with ultraviolet radiation, therefore, the intensity of the field is proportional to its abundance (Meier & Turner 2005; Meier et al. 2015). It is worth noting that we have possible detections of some hydrocarbons that reinforce the idea of the presence of these PDRs.

In Figure 7 we show $R_{12/13}$ vs. HCO^+/HCN and can observe another increasing relation, where the galaxies with values of HCO^+/HCN less than 1 present values of $R_{12/13} < 15$, that is, close to the mean value for nearby starburst galaxies found by Aalto et al. (1995). Note that this ratio is an indicator of the optical depth of the gas, that is, when $R_{12/13}$ increases, the medium becomes optically thicker. Therefore, HCO^+/HCN could be a possible indicator of highly obscured galaxies.

As described above, the integrated molecular gas diagrams cannot offer a diagnosis of the presence or absence of obscured AGNs, as the Sy 1 and Sy 2 galaxies show no differences. However, they can tell us more about the abundance of the molecular gas in terms of the change in density and temperature conditions in the regions near the galactic centers. This can lead to characterization of the conditions of active star formation or its suppression in the regions surrounding an SMBH.

Separating the contribution of the central AGN from the rest of the galaxy is a problem. Observationally, the telescope's main beam is usually larger than the galaxy diameter; hence, the intensity of the lines usually includes contribution of arms (disk) and the bar (if any). In addition to this spatial resolution problem, it is important to detect high tran-

sitions of dense gas tracers with the disadvantage that they are even weaker in intensity than those with rotational transition $J=(1-0)$, when they are optically thin. An example of such a study is reported in Imanishi et al. (2023), a study with ALMA $\lesssim 0.5$ kpc resolution, where they detected the $J=2-1$, $J=3-2$ and $J=4-3$ high transition of several emission lines in 11 ULIRGs and showed the spatial variations of physical and chemical properties of molecular gas within $\lesssim 2$ kpc nuclear regions.

5.3. L_{HCN} vs. L_{IR} Relation

One of the outcomes of the SED fitting analysis is the total infrared luminosity L_{IR} , which is estimated as the sum of torus luminosity L_{TORUS} , and the dust luminosity, L_{DUST} . From the Bayesian analysis values we obtained $\log(L_{\text{IR}}) = 10.96 \pm 0.04 L_{\odot}$ (see Table 7). Sanders et al. (2003) reported a similar value $\log(L_{\text{IR}}) = 10.51 L_{\odot}$ for NGC 4303, determined using the fluxes in all four IRAS bands. Both L_{IR} values were larger than those of Li et al. (2020), who reported $\log(L_{\text{IR}}) = 9.6 \pm 0.03 L_{\odot}$. However, Li et al. (2020) processed calibrated IR image data from Spitzer MIPS and Herschel PACS instruments and corrected to IRAM telescope's main beam (which is close in size to the main beam of the LMT), to estimate L_{IR} . For that reason, we use the value of $\log(L_{\text{IR}})$ from Li et al. (2020), together with our derived value for $\log(L_{\text{HCN}}) = 6.87 \pm 0.08 \text{ K km s}^{-1} \text{ pc}^2$ (Table 3) to place NGC 4303 in figure 2 of Bigiel et al. (2016) and figure 5 of Neumann et al. (2023). In both cases, NGC 4303 lies close to the star formation sequence of a sample of nearby galaxies and individual molecular cloud cores; in the group of active star-forming disk galaxies. As we can see, the L_{HCN} vs. L_{IR} relation presented by Neumann et al. (2023) is independent of disc, arm or interarms regions in spatially resolved galaxies.

From a similar analysis for the galaxy UGC 5101 presented by Cruz-González et al. (2020), which was observed in the same season with the RSR/LTM, we obtain $\log(L_{\text{HCN}}) = 8.87 \pm 0.02 \text{ K km s}^{-1} \text{ pc}^2$ and taking $\log(L_{\text{IR}}) = 11.81 \pm 0.08 L_{\odot}$ from Soifer et al. (1989), this object falls among the Luminous Infrared Galaxies (LIRGs) in the correlation from Bigiel et al. (2016).

5.4. AGN component and SFR in NGC 4303 from SED fitting

According to the results of SED fitting (see Table 7), the AGN component in NGC 4303 is rather low, with an AGN fraction value (fracAGN) of 0.2. Indeed, other studies that use CIGALE to fit AGN

components to SEDs of galaxies have analyzed its reliability in determining the AGN contribution compared with optical classification and color-color diagrams (for example, Wang et al. 2020) and found a minimum value of $\text{fracAGN} = 0.2$ as a reliable lower limit for classifying AGNs using this method. Thus, the value of fracAGN that we find, allows us to classify NGC 4303 at least as marginally AGN, and could be in agreement with the difficulties to classify this galaxy as centrally dominated by star formation or a SMBH, and perhaps is speaking in favor of the fading phase AGN scenario (Esparza-Arredondo et al. 2020).

To assess the goodness of the fit and validate the properties derived from it, we look at the value of the reduced χ^2 , which in our case is 3.1. We consider that this value corresponds to a fairly good fit and confirm this by visual inspection (see Fig. 3). We notice however, that the residuals at far-infrared wavelengths are higher than those at both, shorter and longer (submm) wavelengths, but the model fluxes (red dots) still describe the shape of the observations. This could be caused by the fact that the observation at $100\mu\text{m}$, just before the region of the higher residuals, is very well described by the model (residual ~ 0), hence pinning the model at that point and preventing it from describing the far-infrared observations in a better manner.

Regarding the SFR in NGC 4303, previous works have reported its value estimated using UV and infrared maps. Utomo et al. (2018) estimated the SFR from the combined GALEX FUV map, corrected for galactic extinction, and the WISE W4 infrared map. The maps were convolved to have an angular resolution of $15''$ and background subtracted. After this, they applied the prescriptions described in Kennicutt & Evans (2012) and Jarrett et al. (2013), obtaining a $SFR = 5.24 M_{\odot} \text{ yr}^{-1}$. A similar analysis was done by Chevance et al. (2020) in a FOV of roughly the size of the galaxy (see their Fig. 1), obtaining a $SFR = 4.37 \pm 0.87 M_{\odot} \text{ yr}^{-1}$. Leroy et al. (2019) calibrated the above mentioned prescriptions to match the results from Salim et al. (2016, 2018) who combined GALEX, WISE and SDSS data to estimate the integrated SFR for low-redshift galaxies using CIGALE. The value they found is $SFR = 5.49 \pm 1.58 M_{\odot} \text{ yr}^{-1}$. More recently, Leroy et al. (2021) adopted the prescription of Leroy et al. (2019) using a linear combination of FUV and W4 light, converting the luminosity of each band to SFR using the respective conversion factors and adding the UV and infrared terms to obtain the value $SFR = 5.37 M_{\odot} \text{ yr}^{-1}$.

In summary, previous values of SFR are similar

to our CIGALE value, $SFR = 6.0 \pm 0.3$, but most authors quote somewhat smaller values. We note that our analysis has the advantage that it incorporates UV to mm wavelength photometry, and the clumpy torus component. Assuming that the values of SFR from the literature are the true values, our similar result validates the good quality of our CIGALE fit and the derived properties. Furthermore, using SFR and M_{\star} from (Leroy et al. 2021) we note that NGC 4303 lies along the star-formation main sequence (see for example, Cano-Díaz et al. 2019, for MaNGA SDSS-IV), for nearby galaxies.

6. CONCLUSIONS

With the aim of studying the molecular gas in the obscured core of the galaxy NGC 4303, in this work we analyze the emission line spectrum obtained with the *Redshift Search Receiver* at the Large Millimeter Telescope (in its initial phase of 32 m) in the band of 3 mm (73 - 110 GHz), which correspond to 1.6 kpc centered in the ^{13}CO (110.20 GHz) line.

We detected six molecular lines with $S/N > 3$ in the $J=(1-0)$ rotational transition: C_2H (87.31 GHz), HCN (88.63 GHz), HCO^+ (89.18 GHz), HNC (90.66 GHz), C^{18}O (109.78 GHz) and ^{13}CO (110.20 GHz). The first four lines are gas with critical densities $n_{\text{critic}} > 10^4 \text{ cm}^{-3}$ which makes them ideal for the study of dense gas that is directly responsible for star formation in the galaxy. The average velocities obtained from the Gaussian fit were $151 \pm 29 \text{ km s}^{-1}$ for the diffuse gas, and $178 \pm 60 \text{ km s}^{-1}$ for the dense gas. The result for the diffuse gas velocity is in agreement with the result of Iles et al. (2022), as well as in the observed ^{12}CO $J=(2-1)$ rotation curve of Lang et al. (2020).

The isotopic varieties of carbon monoxide C^{18}O and ^{13}CO trace the diffuse molecular gas with $n_{\text{critic}} \sim 10^3 \text{ cm}^{-3}$ and taking advantage of the fact that the ^{13}CO line is optically thin, that is, $\tau_{13} = 0.09 \pm 0.01$, the column densities relative to ^{12}CO and H_2 for three excitation temperatures (10, 20 and 30 K) were calculated. The results obtained with $T_{\text{ex}} = 30 \text{ K}$ are $N(\text{H}_2) = (5.14 \pm 0.94) \times 10^{21} \text{ cm}^{-2}$ and $M(\text{H}_2) = (1.75 \pm 0.32) \times 10^8 M_{\odot}$ are in good agreement with the expected theory and results obtained by other methods. For example, the last result for the mass of molecular hydrogen is of the same order of magnitude as that found for a central region of $22'' \times 22''$ using a $^{12}\text{CO}(1-0)$ high resolution map obtained by Schinnerer et al. (2002). Using the HCN integrated intensity it was possible to calculate the amount of dense gas in the observed area. The value $M_{\text{dense}} = (4.7 \pm 0.3) \times 10^7 M_{\odot}$ is only 4 times smaller than the amount of gas in H_2 .

The intensities of the emission lines of the dense and diffuse molecular gas tracers clearly show that the abundance with which these species enrich the chemistry of the medium is due to certain star formation activity in the circumnuclear region. PDRs are a consequence of the interaction of young stars or regions of star formation and are responsible for generating this abundance of radicals in a very dense region that would cause them to recombine quickly. The accretion mechanisms of this gas towards the center responsible for such density must be linked to both the spiral arms and the bar that reach the circumnuclear region, which may be influenced by the gravitational potential of the SMBH. Meanwhile, when comparing the line ratios obtained here with those of a sample of galaxies in the literature, no clear trend is observed to distinguish nuclear activity (SF or AGN) from normal galaxies.

Our spectral energy distribution analysis using CIGALE code shows that NGC 4303 has a large clumpy dusty torus, with the following parameters obtained based on the Bayesian analysis: aperture above the equatorial plane $\sigma = 56^\circ \pm 9^\circ$, dust optical depth $\tau_V = 184 \pm 38$, number of dust clouds along the equatorial plane $N_0 = 14 \pm 2$, an inner to outer radius ratio of $Y_{\text{ratio}} = 97 \pm 12$, and a viewing angle of $\text{incl} \sim 70^\circ$. By considering the classical unified AGN model (Antonucci 1993; Urry & Padovani 1995); this viewing angle is in agreement with the Sy 2 classification previously given by Véron-Cetty & Véron (2006).

Furthermore, for NGC 4303 CIGALE yields the total AGN and torus luminosities of $L_{\text{AGN}} = (1.5 \pm 0.6) \times 10^{44} \text{ erg s}^{-1}$, $L_{\text{TORUS}} = (7.1 \pm 2.8) \times 10^{43} \text{ erg s}^{-1}$; while the galaxy dust luminosity is $L_{\text{DUST}} = (2.8 \pm 0.1) \times 10^{44} \text{ erg s}^{-1}$, which yield a total infrared luminosity $L_{\text{IR}} = (3.51 \pm 0.30) \times 10^{44} \text{ erg s}^{-1}$. Finally, the star formation rate obtained is $SFR = 6.0 \pm 0.3 M_\odot/\text{yr}$, which together with the total stellar mass positions this galaxy along the star-formation main-sequence for normal nearby galaxies.

From the molecular gas and dusty torus analysis, we conclude that the central 1.6 kpc emission from NGC 4303 is a mixture of an AGN with a marginal contribution of $\leq 20\%$, most probably a Type 2, with a large clumpy dusty torus and a starburst host galaxy, as evidenced by intense dense molecular gas lines (C_2H , HCN, HCO^+ , and HNC). We found that dense gas contributed significantly to the total molecular gas mass.

Acknowledgements. The authors thank the

referee for a detailed and thorough review of the manuscript and for her/his valuable comments, which have enriched our work and are greatly appreciated. AS acknowledges support from graduate studies scholarship from CONAHCYT and CONAH-CYT/SNI research assistant fellowship. ICG, EB, MHE and AS acknowledge financial support from DGAPA-UNAM grant IN-119123 and CONAHCYT grant CF-2023-G-100. MHE acknowledges financial support from CONAHCYT program *Estancias Posdoctorales por México*. We acknowledge support from CONAHCYT-Mexico, during the construction and Early Science Phase of the Large Millimeter Telescope Alfonso Serrano (LMT/GTM), as well as support from the US National Science Foundation via the University Radio Observatory program, the Instituto Nacional de Astrofísica, Óptica y Electrónica (INAOE), and the University of Massachusetts (UMASS). We also thank LMT/GTM Observatory technical staff during the observations and data processing periods. This research made use of the SIMBAD database, operated at CDS, Strasbourg, France, and the NASA/IPAC Extragalactic Database (NED), which is operated by the Jet Propulsion Laboratory, California Institute of Technology, under contract with the National Aeronautics and Space Administration.

REFERENCES

- Aalto, S., Booth, R. S., Black, J. H., & Johansson, L. E. B. 1995, *A&A*, 300, 369
- Abazajian, K. N., Adelman-McCarthy, J. K., Agüeros, M. A., & et al. 2009, *ApJS*, 182, 543
- Aladro, R., Martín, S., Riquelme, D., & et al. 2015, *A&A*, 579, A101
- Aladro, R., Martín, S., Riquelme, D., & et al. 2015, *Astronomy & Astrophysics*, 579, A101
- Antonucci, R. 1993, *ARA&A*, 31, 473
- Auld, R., Bianchi, S., Smith, & et al. 2013, *VizieR Online Data Catalog*, J/MNRAS/428/1880
- Baan, W. A., Henkel, C., Loenen, A. F., Baudry, A., & Wiklind, T. 2008, *A&A*, 477, 747
- Bai, Y., Zou, H., Liu, J., & Wang, S. 2015, *VizieR Online Data Catalog*, J/ApJS/220/6
- Bendo, G. J., Galliano, F., & Madden, S. C. 2012, *VizieR Online Data Catalog*, J/MNRAS/423/197
- Bennett, C. L., Larson, D., Weiland, J. L., & Hinshaw, G. 2014, *ApJ*, 794, 135
- Bigiel, F., Leroy, A., Walter, F., Brinks, E., de Blok, W. J. G., Madore, B., & Thornley, M. D. 2008, *AJ*, 136, 2846
- Bigiel, F., Leroy, A. K., Jiménez-Donaire, M. J., & et al. 2016, *The Astrophysical Journal*, 822, L26
- Bolatto, A. D., Wolfire, M., & Leroy, A. K. 2013, *ARA&A*, 51, 207

- Boquien, M., Burgarella, D., Roehly, Y., & et al. 2019, *A&A*, 622, A103
- Boselli, A., Voyer, E., Boissier, S., & et al. 2014, *VizieR Online Data Catalog*, J/A+A/570/A69
- Bruzual, G. & Charlot, S. 2003, *MNRAS*, 344, 1000
- Calzetti, D., Armus, L., Bohlin, R. C., & et al. 2000, *ApJ*, 533, 682
- Cano-Díaz, M., Ávila-Reese, V., Sánchez, S. F., & et al. 2019, *MNRAS*, 488, 3929
- Chabrier, G. 2003, *PASP*, 115, 763
- Chen, P. S., Yang, X. H., Liu, J. Y., & Shan, H. G. 2018, *VizieR Online Data Catalog*, J/AJ/155/17
- Chevance, M., Kruijssen, J. M. D., Hygate, & et al. 2020, *MNRAS*, 493, 2872
- Ciesla, L., Boquien, M., Boselli, A., & et al. 2014, *VizieR Online Data Catalog*, J/A+A/565/A128
- Ciesla, L., Charmandaris, V., Georgakakis, A., & et al. 2015, *A&A*, 576, A10
- Colina, L., Piqueras López, J., Arribas, S., Riffel, R., Riffel, R. A., & et al. 2015, *A&A*, 578, A48
- Cortese, L., Boissier, S., Boselli, A., & et al. 2012, *VizieR Online Data Catalog*, J/A+A/544/A101
- Costagliola, F., Aalto, S., Rodríguez, M. I., & et al. 2011, *A&A*, 528, A30
- Cruz-González, I., Gómez-Ruiz, A. I., Caldú-Primo, A., Benítez, E., Rodríguez-Espinosa, J. M., & et al. 2020, *MNRAS*, 499, 2042
- Cybulski, R., Yun, M. S., Erickson, N., & et al. 2016, *MNRAS*, 459, 3287
- Dalya, G., Frei, Z., Galgoczi, G., Raffai, P., & de Souza, R. S. 2016, *VizieR Online Data Catalog*, VII/275
- Dametto, N. Z., Riffel, R., Colina, L., Riffel, R. A., Piqueras López, J., & et al. 2019, *MNRAS*, 482, 4437
- Davis, T. A. 2014, *MNRAS*, 445, 2378
- de Vaucouleurs, G., de Vaucouleurs, A., Corwin, Herold G., J., & et al. 1991, *Third Reference Catalogue of Bright Galaxies*
- Di Francesco, J., Johnstone, D., Kirk, H., MacKenzie, T., & Ledwosinska, E. 2008, *ApJS*, 175, 277
- Dickman, R. L. 1978, *ApJS*, 37, 407
- Erickson, N., Narayanan, G., Goeller, R., & Grosslein, R. A. J. Baker, J. Glenn A. Harris J. G. Mangum & M. S. Yun, 71
- Esparza-Arredondo, D., Osorio-Clavijo, N., González-Martín, O., & et al. 2020, *ApJ*, 905, 29
- Fazio, G. G., Hora, J. L., Allen, L. E., & et al. 2004, *ApJS*, 154, 10
- Filippenko, A. V. & Sargent, W. L. W. 1985, *ApJS*, 57, 503
- Frei, Z., Guhathakurta, P., Gunn, J. E., & Tyson, J. A. 1996, *AJ*, 111, 174
- Fritz, J., Franceschini, A., & Hatziminaoglou, E. 2006, *MNRAS*, 366, 767
- Gao, Y. & Solomon, P. M. 2004a, *ApJS*, 152, 63
- . 2004b, *ApJ*, 606, 271
- García-Burillo, S. *IAU Symposium*, Vol. 315, , From Interstellar Clouds to Star-Forming Galaxies: Universal Processes?, ed. P. Jablonka P. André & F. van der Tak, 207–214
- Graciá-Carpio, J., García-Burillo, S., Planesas, P., & Colina, L. 2006, *ApJ*, 640, L135
- Griffin, M. J., Abergel, A., Abreu, A., & et al. 2010, *A&A*, 518, L3
- Hirota, T., Yamamoto, S., Mikami, H., & Ohishi, M. 1998, *ApJ*, 503, 717
- Holland, W. S., Robson, E. I., Gear, W. K., & et al. 1999, *MNRAS*, 303, 659
- Hönig, S. F. & Kishimoto, M. 2017, *ApJ*, 838, L20
- Huchra, J. P., Wyatt, W. F., & Davis, M. 1982, *AJ*, 87, 1628
- Iles, E. J., Pettitt, A. R., & Okamoto, T. 2022, *MNRAS*, 510, 3899
- Imanishi, M., Baba, S., Nakanishi, K., & Izumi, T. 2023, *ApJ*, 954, 148
- Israel, F. P. 2020, *A&A*, 635, A131
- Jarrett, T. H., Masci, F., Tsai, C. W., & et al. 2013, *AJ*, 145, 6
- Jiang, X., Wang, J., & Gu, Q. 2011, *MNRAS*, 418, 1753
- Jiménez-Bailón, E., Santos-Lleó, M., Mas-Hesse, J. M., Guainazzi, M., Colina, L., Cerviño, M., & González Delgado, R. M. 2003, *ApJ*, 593, 127
- Jiménez-Donaire, M. J. 2017, PhD thesis, Ruprecht-Karls University of Heidelberg, Germany
- Jiménez-Donaire, M. J., Bigiel, F., Leroy, A. K., & et al. 2017, *MNRAS*, 466, 49
- . 2019, *ApJ*, 880, 127
- Jones, A. P., Köhler, M., Ysard, N., Bocchio, M., & Verstraete, L. 2017, *A&A*, 602, A46
- Keene, J., Schilke, P., Kooi, J., Lis, D. C., Mehringer, D. M., & Phillips, T. G. 1998, *ApJ*, 494, L107
- Kennicutt, R. C. & Evans, N. J. 2012, *ARA&A*, 50, 531
- Kim, S., Rey, S.-C., Jerjen, H., Lisker, T., Sung, E.-C., Lee, Y., Chung, J., Pak, M., Yi, W., & Lee, W. 2014, *ApJS*, 215, 22
- Kohno, K. *Astronomical Society of the Pacific Conference Series*, Vol. 289, , The Proceedings of the IAU 8th Asian-Pacific Regional Meeting, Volume 1, ed. S. Ikeuchi J. Hearnshaw & T. Hanawa, 349–352
- Kohno, K., Matsushita, S., Vila-Vilaró, B., & et al. *The Central Kiloparsec of Starbursts and AGN: The La Palma Connection*, ed. , J. H. Knapen J. E. Beckman I. Shlosman & T. J. Mahoney, 672
- Lang, P., Meidt, S. E., Rosolowsky, E., Nofech, J., & et al. 2020, *The Astrophysical Journal*, 897, 122
- Lee, C., Chung, A., Yun, M. S., & et al. 2014, *MNRAS*, 441, 1363
- Leroy, A. K., Sandstrom, K. M., Lang, D., Lewis, A., Salim, S., Behrens, E. A., Chastenet, J., Chiang, I.-D., Gallagher, M. J., Kessler, S., & Utomo, D. 2019, *ApJS*, 244, 24
- Leroy, A. K., Schinnerer, E., Hughes, A., & et al. 2021, *ApJS*, 257, 43
- Leroy, A. K., Usero, A., Schrubba, A., & et al. 2017, *ApJ*, 835, 217
- Li, F., Wang, J., Fang, M., Tan, Q.-H., Zhang, Z.-Y., Gao, Y., & Li, S. 2020, *Publications of the Astro-*

- nomical Society of Japan, 72
- Li, F., Wang, J., Gao, F., & et al. 2021, *Monthly Notices of the Royal Astronomical Society*, 503, 4508
- Loenen, A. F., Spaans, M., Baan, W. A., & Meijerink, R. 2008, *A&A*, 488, L5
- Malkan, M. A., Jensen, L. D., Rodriguez, D. R., Spinoglio, L., & Rush, B. 2017, *ApJ*, 846, 102
- Martin, D. C., Fanson, J., Schiminovich, D., & et al. 2005, *ApJ*, 619, L1
- Martín, S., Kohno, K., Izumi, T., & et al. 2015, *A&A*, 573, A116
- Meier, D. S. & Turner, J. L. 2005, *ApJ*, 618, 259
- Meier, D. S., Walter, F., Bolatto, A. D., & et al. 2015, *The Astrophysical Journal*, 801, 63
- Meijerink, R. & Spaans, M. 2005, *A&A*, 436, 397
- Meijerink, R., Spaans, M., & Israel, F. P. 2007, *A&A*, 461, 793
- Miyaji, T., Herrera-Endoqui, M., Krumpe, M., & et al. 2019, *ApJ*, 884, L10
- Morokuma-Matsui, K., Sorai, K., Sato, Y., & et al. 2020, *Publications of the Astronomical Society of Japan*, 72
- Moustakas, J. & Kennicutt, Jr., R. C. 2006, *ApJS*, 164, 81
- Nakajima, T., Takano, S., Kohno, K., Harada, N., & Herbst, E. 2018, *PASJ*, 70, 7
- Nenkova, M., Sirocky, M., Ivezić, Z., & Elitzur, M. 2008, *The Astrophysical Journal*, 685
- Nenkova, M., Sirocky, M. M., Ivezić, Ž., & Elitzur, M. 2008a, *ApJ*, 685, 147
- Nenkova, M., Sirocky, M. M., Nikutta, R., Ivezić, Ž., & Elitzur, M. 2008b, *ApJ*, 685, 160
- Neugebauer, G., Habing, H. J., van Duinen, R., & et al. 1984, *ApJ*, 278, L1
- Neumann, L., Gallagher, M. J., Bigiel, F., & et al. 2023, *MNRAS*, 521, 3348
- Nishimura, Y., Aalto, S., Gorski, M. D., & et al. 2024, *arXiv e-prints*, arXiv:2402.15436
- Pilbratt, G. L., Riedinger, J. R., Passvogel, T., & et al. 2010, *A&A*, 518, L1
- Poglitsch, A., Waelkens, C., Geis, N., & et al. 2010, *A&A*, 518, L2
- Privon, G. C., Ricci, C., Aalto, S., & et al. 2020, *ApJ*, 893, 149
- Rahman, N., Helou, G., & Mazzarella, J. M. 2006, *ApJ*, 652, 1068
- Riffel, R. A., Colina, L., Storchi-Bergmann, T., & et al. 2016, *MNRAS*, 461, 4192
- Rybak, M., Hodge, J. A., Greve, T. R., & et al. 2022, *A&A*, 667, A70
- Salim, S., Boquien, M., & Lee, J. C. 2018, *ApJ*, 859, 11
- Salim, S., Lee, J. C., Janowiecki, S., da Cunha, E., Dickinson, M., Boquien, M., Burgarella, D., Salzer, J. J., & Charlot, S. 2016, *ApJS*, 227, 2
- Sanders, D. B., Mazzarella, J. M., Kim, D.-C., Surace, J. A., & Soifer, B. T. 2003, *AJ*, 126, 1607
- Sandstrom, K. M., Leroy, A. K., Walter, F., & et al. 2013, *ApJ*, 777, 5
- Santos, D. J. D., Goto, T., Kim, S. J., & et al. 2021, *MNRAS*, 507, 3070
- Schinnerer, E., Maciejewski, W., Scoville, N., & Moustakas, L. A. 2002, *ApJ*, 575, 826
- Sheth, K., Regan, M., Hinz, J. L., & et al. 2010, *PASP*, 122, 1397
- Skrutskie, M. F., Cutri, R. M., Stiening, R., & et al. 2006, *AJ*, 131, 1163
- Snell, R. L., Narayanan, G., Yun, M. S., & et al. 2011, *AJ*, 141, 38
- Soifer, B. T., Boehmer, L., Neugebauer, G., & Sanders, D. B. 1989, *AJ*, 98, 766
- Solomon, P. M., Downes, D., Radford, S. J. E., & Barrett, J. W. 1997, *ApJ*, 478, 144
- Sorai, K., Kuno, N., & et al. 2019, *Publications of the Astronomical Society of Japan*
- Stassun, K. G. 2019, *VizieR Online Data Catalog*, IV/38
- Strong, A. W., Bloemen, J. B. G. M., Dame, T. M., & et al. 1988, *A&A*, 207, 1
- Teng, Y.-H., Sandstrom, K. M., Sun, J., & et al. 2023, *The Astrophysical Journal*, 950, 119
- Teng, Y.-H., Sandstrom, K. M., Sun, J., Leroy, A. K., Johnson, L. C., & et al. 2022, *The Astrophysical Journal*, 925, 72
- Urry, C. M. & Padovani, P. 1995, *PASP*, 107, 803
- Usero, A., Leroy, A. K., Walter, F., Schrubba, A., García-Burillo, S., & et al. 2015, *AJ*, 150, 115
- Utomo, D., Sun, J., Leroy, A. K., & et al. 2018, *ApJ*, 861, L18
- Veron-Cetty, M. P. & Veron, P. 1986, *A&AS*, 66, 335
- Véron-Cetty, M.-P. & Véron, P. 2006, *A&A*, 455, 773
- Wang, T.-W., Goto, T., Kim, S. J., & et al. 2020, *MNRAS*, 499, 4068
- Werner, M. W., Roellig, T. L., Low, F. J., & et al. 2004, *ApJS*, 154, 1
- Wilson, T. L. & Rood, R. 1994, *ARA&A*, 32, 191
- Wright, E. L. 2006, *PASP*, 118, 1711
- Wright, E. L., Eisenhardt, P. R. M., Mainzer, A. K., & et al. 2010, *AJ*, 140, 1868
- Wu, J., Evans, Neal J., I., Gao, Y., Solomon, P. M., Shirley, Y. L., & Vanden Bout, P. A. 2005, *ApJ*, 635, L173
- Wu, J., Evans, Neal J., I., Shirley, Y. L., & Knez, C. 2010, *ApJS*, 188, 313
- Yajima, Y., Sorai, K., Kuno, N., Muraoka, K., & et al. 2019, *PASJ*, 71, S13
- Yamada, S., Ueda, Y., Herrera-Endoqui, M., & et al. 2023, *ApJS*, 265, 37
- Yun, M. S., Aretxaga, I., Gurwell, M. A., & et al. 2015, *MNRAS*, 454, 3485
- Yun, M. S., Reddy, N. A., & Condon, J. J. 2001, *ApJ*, 554, 803
- Zurita, A., Florido, E., Bresolin, F., Pérez-Montero, E., & Pérez, I. 2021, *MNRAS*, 500, 2359

TABLE 5
PHOTOMETRY USED IN THE SED FITTING WITH CIGALE.

| Band | λ_{eff} (μm) | Flux [†] (mJy) | Telescope/Instrument or Survey | Res. ^{††} ($''$) | FOV ($'$) | Ref. |
|-----------|---|----------------------------|-----------------------------------|--------------------------------|----------------|------|
| FUV | 0.153 | 41.3±1.9 | GALEX | 5.3 | 72.0 | 1 |
| NUV | 0.231 | 61.0±1.7 | GALEX | 5.3 | 72.0 | 1 |
| u | 0.352 | 158.0±5.0 | SDSS | ≤ 1.5 | 180.0 | 2 |
| g | 0.482 | 392.0±7.0 | SDSS | ≤ 1.5 | 180.0 | 2 |
| r | 0.625 | 628.0±12.0 | SDSS | ≤ 1.5 | 180.0 | 2 |
| i | 0.763 | 819.0±15.0 | SDSS | ≤ 1.5 | 180.0 | 2 |
| z | 0.902 | 982.0±28.0 | SDSS | ≤ 1.5 | 180.0 | 2 |
| J | 1.2 | 1300.0±20.0 | 2MASS | 2.0 | 8.5 | 3 |
| H | 1.6 | 1320.0±20.0 | 2MASS | 2.0 | 8.5 | 4 |
| Ks | 2.2 | 1240.0±-999.0 | 2MASS | 2.0 | 8.5 | 5 |
| W1 | 3.35 | 578.0±-999.0 | WISE | 6.1 | 47.0 | 5 |
| IRAC1 | 3.6 | 714.0±1.0 | Spitzer/IRAC | 1.7 | 5.0 | 6 |
| IRAC2 | 4.5 | 479.0±1.0 | Spitzer/IRAC | 1.6 | 5.0 | 6 |
| W2 | 4.60 | 370.0±-999.0 | WISE | 6.4 | 47.0 | 5 |
| IRAC4 | 8.0 | 3300.0±410.0 | Spitzer/IRAC | 1.9 | 5.2×5.2 | 7 |
| W3 | 12 | 4180.0±110.0 | WISE | 6.5 | 47.0 | 7 |
| IRAS1 | 12 | 3210.0±50.0 | IRAS | 30.0 | 63.6 | 8 |
| W4 | 22 | 4160.0±190.0 | WISE | 12.0 | 47.0 | 9 |
| MIPS24 | 24 | 3940.0±160.0 | Spitzer/MIPS | 6.0 | 5.4×5.4 | 10 |
| IRAS2 | 25 | 4900.0±-999.0 | IRAS | 30.0 | 63.6 | 11 |
| IRAS3 | 60 | 37300.0±-999.0 | IRAS | 60.0 | 63.6 | 11 |
| PACSgreen | 100 | 97900.0±11800.0 | Herschel/PACS | 8.0 | 3.5×1.75 | 12 |
| IRAS4 | 100 | 79700.0±-999.0 | IRAS | 120.0 | 63.6 | 13 |
| MIPS160 | 160 | 99800.0±12000.0 | Spitzer/MIPS | 38.0 | 2.1×5.3 | 10 |
| PACSred | 160 | 107000.0±13000.0 | Herschel/PACS | 13.0 | 3.5×1.75 | 12 |
| PWS | 250 | 55200.0±3900.0 | Herschel/SPIRE | 18.0 | 8.0×4.0 | 14 |
| PWM | 350 | 22800.0±1600.0 | Herschel/SPIRE | 25.0 | 8.0×4.0 | 14 |
| PWL | 500 | 8100.0±580.0 | Herschel/SPIRE | 36.0 | 8.0×4.0 | 14 |
| SCUBA2 | 850 | 705.0±20.0 | JCMT/SCUBA | 22.9 | 2.3 | 15 |

REFERENCES: (1) Cortese et al. (2012); (2) Kim et al. (2014); (3) Bai et al. (2015); (4) Dalya et al. (2016); (5) Stassun (2019); (6) Sheth et al. (2010); (7) Ciesla et al. (2014); (8) Moustakas & Kennicutt (2006); (9) Boselli et al. (2014); (10) Bendo et al. (2012); (11) Rahman et al. (2006); (12) Auld et al. (2013); (13) Yun et al. (2001); (14) Chen et al. (2018); (15) Di Francesco et al. (2008).

[†]The flux data without error (-999.0) are taken as upper limits in the SED fitting analysis (green upside down triangles in Fig. 3).

^{††}Telescope resolution.

TABLE 6
PARAMETERS USED IN THE SED FITTING WITH CIGALE.

| Component | Module | Parameter | Values |
|------------------|------------------|------------------------|--|
| SFH | sfhdelayed | tau_main | 1000, 2000, 4000, 6000 (Myr) |
| | | age_main | 1500, 4000, 8000 (Myr) |
| | | tau_burst | 10, 25 (Myr) |
| | | age_burst | 10, 20 (Myr) |
| | | f_burst | 0.0, 0.01 |
| Stellar emission | bc03 | imf | Chabrier (2003) |
| | | metallicity | 0.0001, 0.0004, 0.004, 0.008, 0.02, 0.05 |
| | | separation_age | 10 (Myr) |
| Nebular emission | nebular | logU | -2.0 |
| | | f_esc | 0.0 |
| | | f_dust | 0.0 |
| | | lines_width | 300.0 |
| Attenuation law | dustatt_modified | E_BV_lines | 0.0, 0.3, 0.6, 0.9, 1.2, 1.5, 1.8, 2.1, 2.4 |
| | | E_BV_factor | 0.44 |
| | | uv_bump_wavelength | 217.5 |
| | | uv_bump_width | 35.0 |
| | | uv_bump_amplitude | 0, 1.5, 3 |
| | | powerlaw_slope | -0.2, 0 |
| | | Ext_law_emission_lines | 1 (MW) |
| Rv | 3.1 | | |
| Dust emission | themis | qhac | 0.06, 0.17, 0.36 |
| | | umin | 0.1, 1.0, 10.0, 50.0 |
| | | alpha | 1.0, 2.0, 3.0 |
| | | gamma | 0.1, 0.25 |
| AGN | nenkova2008 | Y_ratio | 5, 10, 30, 60, 100 |
| | | op_angle | 20, 40, 60 |
| | | tau_V | 20, 60, 80, 120, 200 |
| | | N_0 | 3, 5, 10, 15 |
| | | incl | 10, 30, 60, 80 |
| | | q | 0.0, 0.5, 1.0, 2.0, 3.0 |
| | | fracAGN | 0.0, 0.1, 0.2, 0.3, 0.4, 0.5, 0.6, 0.7, 0.8, 0.9 |

TABLE 7
RESULTS FOR THE AGN AND DUSTY TORUS PROPERTIES
AFTER THE SED FITTING WITH CIGALE.

| Parameter | Best fit result | Bayessian analysis |
|---|----------------------|----------------------------------|
| <i>Y_ratio</i> | 100 | 97 ± 12 |
| <i>op_angle</i> ($^{\circ}$) | 60 | 56 ± 9 |
| <i>tau_V</i> | 200 | 184 ± 38 |
| <i>N_0</i> | 15 | 14 ± 2 |
| <i>incl</i> ($^{\circ}$) | 80 | 67 ± 16 |
| <i>q</i> | 0.0 | 0.12 ± 0.29 |
| <i>fracAGN</i> | 0.2 | 0.20 ± 0.07 |
| <i>SFR</i> ($M_{\odot} \text{ yr}^{-1}$) | 6.0 | 6.0 ± 0.3 |
| <i>L</i> _{AGN} (erg s^{-1}) | 1.5×10^{44} | $(1.5 \pm 0.6) \times 10^{44}$ |
| <i>L</i> _{TORUS} (erg s^{-1}) | 7.0×10^{43} | $(7.1 \pm 2.8) \times 10^{43}$ |
| <i>L</i> _{DUST} (erg s^{-1}) | 2.8×10^{44} | $(2.8 \pm 0.1) \times 10^{44}$ |
| <i>L</i> _{IR} = (erg s^{-1}) | 3.5×10^{44} | $(3.51 \pm 0.30) \times 10^{44}$ |

TABLE 8
MOLECULAR LINE TRANSITIONS DETECTED IN NGC 4303 AND OTHER GALAXIES

| Galaxy | $\frac{\text{C}_2\text{H}}{\text{HCO}^+}$ | $\frac{\text{C}_2\text{H}}{\text{HCN}}$ | $\frac{\text{HCN}}{\text{HCO}^+}$ | $\frac{\text{HNC}}{\text{HCO}^+}$ | $\frac{\text{HCN}}{^{12}\text{CO}}$ | Activity* | Reference** |
|----------|---|---|-----------------------------------|-----------------------------------|-------------------------------------|-----------|-------------|
| NGC 4303 | 0.55 | 0.50 | 1.10 | 0.64 | 0.03 | Sy2 | a |
| UGC 5101 | 0.84 | 0.56 | 1.50 | 0.83 | 0.10 | Sy1.5 | b |
| IC 180 | 2.65 | 1.66 | 1.60 | 0.86 | - | - | c |
| NGC 1614 | 0.26 | 0.54 | 0.74 | 0.22 | 0.02 | Sy2 | c |
| NGC 3079 | 0.48 | 0.54 | 0.89 | 0.24 | 0.02 | Sy2 | c |
| NGC 4194 | 0.73 | 0.96 | 0.76 | 0.40 | 0.02 | - | c |
| NGC 4388 | 0.14 | 0.19 | 0.73 | 0.30 | - | Sy2 | c |
| NGC 4418 | 0.25 | 0.15 | 1.69 | 0.79 | - | Sy2 | c |
| NGC 6090 | 0.27 | 0.46 | 0.60 | 0.15 | - | Sy2 | c |
| NGC 6240 | 0.21 | 0.34 | 0.61 | 0.12 | 0.04 | Sy2 | c |
| NGC 7771 | 0.29 | 0.26 | 1.10 | 0.65 | 0.03 | - | c |
| NGC 660 | 0.43 | 0.45 | 0.96 | 0.50 | 0.03 | Sy2 | c |
| NGC 3556 | 0.99 | 1.56 | 0.64 | 0.19 | 0.01 | - | d |
| NGC 2273 | - | - | 1.67 | 1.00 | 0.03 | Sy1-2 | d |
| NGC 5236 | 0.43 | 0.39 | 1.09 | 0.44 | 0.05 | SB | e |
| NGC 253 | 0.60 | 0.51 | 1.18 | 0.61 | 0.07 | Sy2 | e |
| M82 | 0.61 | 0.87 | 0.70 | 0.31 | 0.03 | SB | e |
| M51 | 0.47 | 0.23 | 2.02 | 0.67 | 0.11 | - | e |
| NGC 1068 | 0.54 | 0.33 | 1.64 | 0.54 | 0.14 | Sy2 | e |
| NGC 7469 | 0.55 | 0.67 | 0.82 | 0.37 | 0.04 | Sy1.2 | e |
| ARP 220 | 0.83 | 0.35 | 2.39 | 1.68 | 0.12 | Sy2 | e |
| MRK 231 | 0.43 | 0.28 | 1.54 | 0.51 | 0.16 | Sy1 | e |
| IC 342 | 0.25 | 0.18 | 1.38 | 0.54 | 0.07 | SB | f |

Notes: *Activity type from NASA/IPAC Extragalactic Database (NED).

**Dense gas emission line ratios from: ^a This work, ^b Cruz-González et al. (2020), ^c Jiang et al. (2011), ^d Costagliola et al. (2011), ^e Aladro et al. (2015), ^f Nakajima et al. (2018).